# Efficient, Stable Infrared Photovoltaics based on Solution-Cast PbSe Colloidal Quantum Dots

By

Ghada I. Koleilat

A thesis submitted in conformity with the requirements
for the degree of Master of Applied Science
Graduate Department of Electrical and Computer Engineering
University of Toronto

# ABSTRACT

## Efficient, Stable Infrared Photovoltaics based on Solution-Cast PbSe Colloidal Quantum Dots

Ghada I. Koleilat

Master of Applied Science

Graduate Department of Electrical and Computer Engineering

University of Toronto

2008

Half of the sun's power lies in the infrared. As a result, the optimal bandgaps for solar cells in both the single-junction and even the tandem architectures lie beyond 850 nm. However, progress in low-cost, large-area, physically-flexible solar cells has instead been made in organic and polymer materials possessing absorption onsets in the visible. Recent advances have been achieved in solution-cast infrared photovoltaics through the use of colloidal quantum dots. Here we report stable solution-processed photovoltaic devices having 3.6% power conversion efficiency in the infrared. The use of a strongly-bound bidentate linker, benzenedithiol, ensures device stability over weeks. We investigate in detail the physical mechanisms underlying the operation of this class of device. We find that diffusion of electrons and holes over hundreds of nanometers through our PbSe colloidal quantum dot solid is chiefly responsible for the high external quantum efficiencies obtained in this new class of devices.

# Acknowledgements

I would like to thank my supervisor, Prof. Edward Sargent, for his invaluable guidance and support throughout the course of my graduate studies. I am deeply grateful for the great opportunity he offered me to be part of his first-class research team. I also want to thank him for his generous financial support and his assistance in writing this thesis.

I also would like to thank Dr. Andras Pattantyus-Abraham for his continual guidance; his insights were always a source of inspiration to my research work. He is an exceptional researcher and I am very grateful to be learning from his expertise.

I am also grateful to Dr. Larissa Levina for her patience and collaborative effort, especially in developing and optimizing a new chemical processing strategy for the nanocrystals reported herein. She has been a great mentor throughout this project.

I would like to thank Leyla Soleymani for her constant support and friendship; I also thank all the wonderful members of the Sargent group for their help and for providing a warm work environment: Sean Hinds, Gerasimos Konstantanos, Jason Clifford, Ethan Klem, Keith Johnston, Harnik Shukla, Stefan Myrskog, Jiang Tang, Aaron Barkhouse, Armin Fischer, Vlad Sukhovatkin, and Ian Adams.

I would also like to express my deepest gratitude to my parents without whom I would not be where I am today. I would like to give a special thank you to my older brother and best friend, Walid, who has been there for me all my life. I wouldn't have made it through far away from home without his constant support.

# Table of Contents

# List of Figures

# List of Tables

# 1 Introduction

## 1.1 Motivation

The research reported herein is motivated by the urgent need to answer the following questions: Why do we need renewable energies? How can we meet our future energy demands using green resources? Why research in infrared solution-processed photovoltaics is strongly needed?

### 1.1.1 Solar Energy

*"Sustainable development is development that meets the needs of the present without compromising the ability of future generations to meet their own needs [1]."*

The energy economy of most industrialized countries today is primarily dependent on fossil energy in the form of coal, oil, and natural gas; these provide 80% of the present world energy supply [2]. The world's energy demand is projected to double by 2050, particularly due to growing importance of energy consumption in developing countries. Fossil fuels cannot be considered the world's main source of energy for long because of their expected short lifetime and their current high consumption rate. The high oil price today also needs to be weighted in the current energy crisis. The ongoing rise of the latter is due to multiple factors; it is first an indication that natural resources are not abundant and cheap anymore, and it is also a direct consequence of the global

geopolitical conflicts. Furthermore, concerns are raised about the role of fossil fuel consumption, and the burning of green house gases in climate change; already natural disasters, attributed to global warming, have been occurring all over the world [3].

The energy challenges that the world faces today will only be resolved if we change the course and move toward more sustainable energy solutions. In the midst of 1970's fuel crisis, modern renewable energy resources for electrical power generation such as wind power, photovoltaic, and geothermal energy were considered as an untapped potential and candidates for green clean energy supply [3]. The Brundtland report states that these renewable sources "offer the world potentially huge primary energy sources, sustainable in perpetuity and available in one way or another to every nation on Earth [1]."

Among renewable energies, solar energy is the largest and the only abundant and equitable resource with the capacity to meet a large part of our society's future power needs. The sun can potentially supply 2000 times as much energy as the world consumes yearly [4]. In fact, harvesting solar energy at 10% efficiency using only 1% of the world land area would potentially supply us with twice our current energy needs [5].

Photovoltaic energy conversion is an elegant one-step process where incoming solar radiation is directly converted into electricity without emission of any hazardous byproducts. Although sunlight is diffuse, it is vast and essentially unlimited [4]. Solar cells are also safe, modular, easily installed at any point-of-use, and integrated into any structure [4]. Although the fabrication cost of conventional photovoltaic devices is still high, solar power is predicted to become a strong viable alternative to fossil fuel energy before 2050.

### 1.1.2 The Need for Solution Processed Materials

In 1839, nineteen year-old Edmund Bequerel was the first to report the photovoltaic effect when he discovered that silver chloride responded to light [6]. The first solid state photovoltaic devices were constructed in 1876; a rectifying junction formed between a semiconductor and a metal. It wasn't until the 1950's that p-n junctions in silicon were manufactured following the development of silicon electronics. The first silicon solar cell was fabricated in 1954 at Bell labs. The efficiency improved over the following decades but the production cost estimated at $200 per Watt was way too high to consider in power generation applications. Over the past thirty years, solar cell efficiencies have risen past 30%; however, mass production is still hindered by either the high material cost and the limited resources available, or the complicated architectures.

Current research has been aimed toward the exploration of new materials as a viable alternative to silicon in the fabrication of solar cells. Solution-processed photovoltaics offer solar energy harvesting characterized by low cost, ease of processing, physical flexibility, and large area coverage. Conjugated polymers [7], inorganic nanocrystals (NCs) [8], and hybrid materials [9] have been widely investigated and optimized to this purpose. If high solar efficiencies are achieved with these inexpensive materials that require simple deposition techniques such as spin-coating, drop-casting, or inkjet printing, major strides in the energy industry could be achieved.

### 1.1.3 Importance of Infrared Power Conversion

The infrared region of the electromagnetic spectrum is invaluable in many applications. Infrared-sensitive materials range from inorganic bulk semiconductors to

quantum confined nanocrystals with tunable optical properties. In the area of optical sensing, thermal imaging and biological imaging, detection of near-infrared wavelengths is essential. Of particular interest, infrared-sensitive materials are used in photoconductive devices that detect light and in solar cells that convert light into electricity [10,11,12].

The air mass factor describes the attenuation and scattering experienced by the solar spectrum reaching the earth's surface and caused by the atmosphere's constituents [6]. The Air mass 1.5 (AM1.5), the conventional spectrum used in the photovoltaic industry, corresponds to the sun being at an angle of elevation of $42^0$ and at an integrated power density of 100 mW $cm^{-2}$. Referring to the AM1.5 spectrum depicted in figure 1.1, half of the sun's power lies in the infrared. As a result, the optimal bandgaps for solar cells in both the single-junction and even the tandem architectures lie beyond 850 nm. High efficiency multijunction solar cells offer the prospect of exceeding 40% efficiency [13] through the inclusion of infrared-bandgap materials. For double and triple junction solar cells, the smallest-bandgap junction optimally lies at 1320 nm and 1750 nm respectively [13]. It is therefore essential to harness the infrared portion of the solar spectrum [14,15,16].

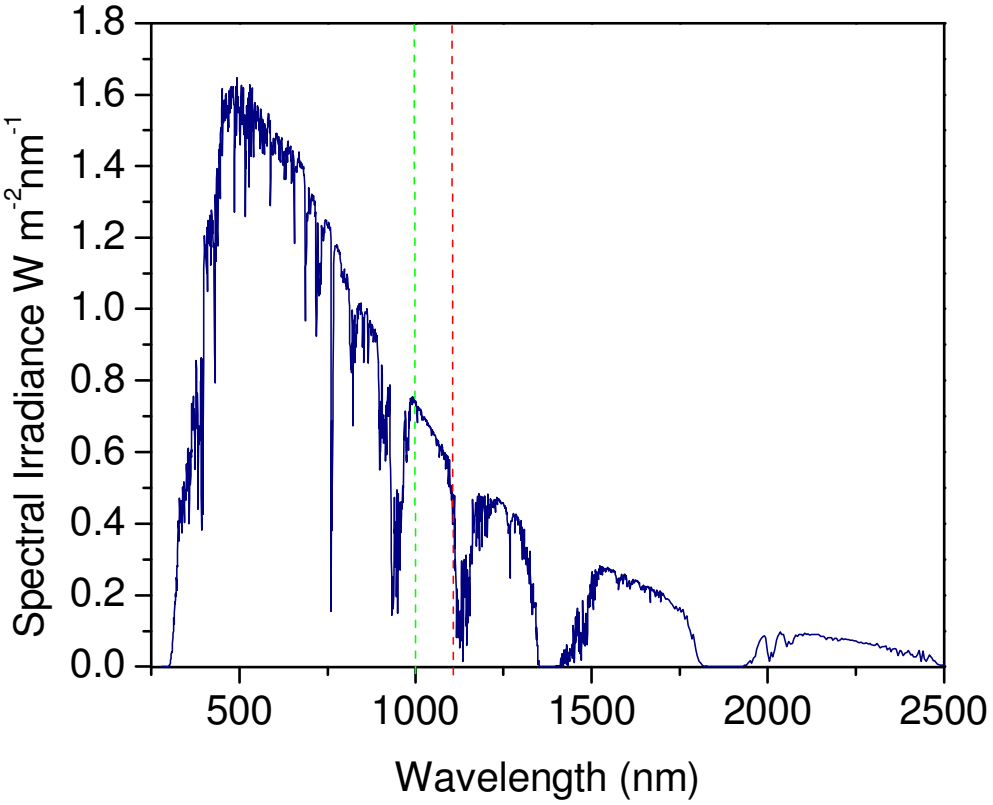


**Figure 1-1 AM1.5 solar spectrum. The dashed green line represents the limit of organic solar cells sensitivity and the dashed red line the Si absorption onset. The irradiance beyond 1000 nm constitutes one third of the total solar power.**

## 1.2 Thesis Statement

**The objective of this thesis is the demonstration of the first stable efficient infrared solution processed photovoltaic devices based on crosslinked PbSe nanocrystals.**

The optimizations of the chemical processes leading to efficient photovoltaic devices are reported herein. We report the first PbSe colloidal quantum photovoltaic to exceed one percent power conversion efficiency [17,18]. It is also the first reported solution-processed infrared photovoltaic device to be stable over weeks.

### 1.2.1 Organization

Chapter 2 will focus on presenting a literature review to position our work within the context of other related research. It also serves as a background reference on the solar cell concepts that will be used throughout this report. In chapter 3, we will describe the solution processing of our material, its synthesis and the optimized ligand exchange that resulted in stably suspended PbSe nanocrytals in solution. Chapter 4 will describe the film deposition process, the initial limitations we faced, and the strategy we devised to overcome them. The optimized chemical crosslinking treatment will be detailed in chapter 4. Chapter 5 will be dedicated to present the photovoltaic devices performance, and their stability. We will also describe the characterization techniques we used to determine the various transport properties of our nanocrystal films in this chapter. In chapter 6, we present a detailed investigation of the physical mechanisms responsible for the performance of our devices and attempt to explain the origins of high efficiencies in our devices, from the role of the Shottky junction and dominant transport mechanism to the role of the benzendithiol crosslinking molecule. The final chapter 7 summarizes this work. Appendix A and B summarize the material used, their sources, and present explicit details about the measurement techniques.

# 2 Literature Review

In the previous chapter, we explained the motivation behind the use of infrared sensitive solution processed materials in photovoltaics. The following chapter aims foremost to position this research within the context of other work in related areas. We examine the theoretical concepts and device architectures of solution-processed materials: the visible active conjugated polymers and the infrared-sensitive lead salt quantum dots. The chapter also serves as an overview of essential solar cell and metal/semiconductor junction concepts. We present the strategy pursued in this work at the end of the chapter.

## 2.1 Solar Cell Concepts

Two forms of solar converters can be fabricated: thermal converter where solar radiation is transformed to thermal energy and quantum converter where the electrical output can be extracted directly from the light absorber. In the latter, a photon excites an electron from the valence band to the conduction band. Electrons and holes are separated before they can relax by a built-in asymmetry to produce an external current through the load, resulting in electrical power generation [5, 6]. The power output of the solar cell is the product of the flow of photo-exited carriers which is the current, and the driving force for the flow which is directly related to the potential difference [5].

### 2.1.1 Important Definitions

When the terminals of a solar cell are isolated, the voltage across the terminals is the open circuit voltage $V_{oc}$. When the terminals are connected together, the flowing current is the short circuit current $I_{sc}$; the short circuit current density $J_{sc}$ is the standard figure of merit used for comparison.

When a load is connected to the terminals of the solar cell in the dark, the current is called the dark current $I_{dark}$. Solar cells behave like diodes in the dark where the forward bias current is much larger than the reverse bias current. Ideally, the dark current density $J_{dark}$ (V) is expressed as

$$J_{dark}(V) = J_0(e^{qV/k_BT} - 1)$$

where $J_0$ is a constant, $k_B$ is Boltzmann's constant and T is the temperature in degrees Kelvin [6].

The net current response can be approximated as the superposition of the short circuit current and the dark current

$$J(V) = J_{sc} - J_{dark}(V) = J_{sc} - J_0(e^{qV/k_BT} - 1)$$

When the terminals are isolated, the dark current and the short circuit photocurrent cancel each other out and the open circuit voltage is expressed as

$$V_{oc} = k_BT/q \ln (J_{sc}/J_0 - 1)$$

The solar cell delivers power to the external circuit when its bias ranges from 0 to $V_{oc}$. The power density P is the product of the circuit current density and the voltage across the terminals. The maximum power point occurs at $V_m$ and $J_m$ as indicated in Figure 2.1.

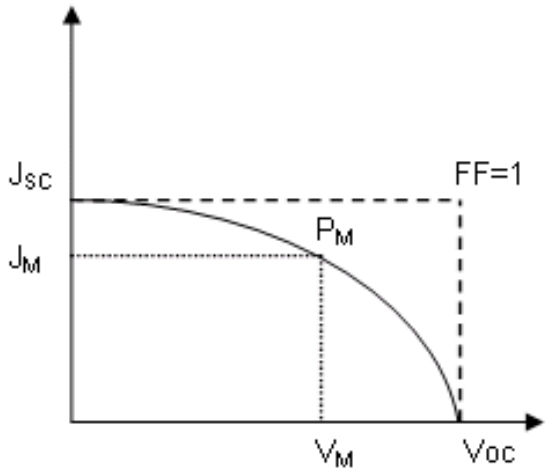


**Figure 2-1 Current-Voltage characteristics of a typical solar cell**

The fill factor is a figure of merit describing the 'squareness' of the J-V curve and is defined as

$$FF = J_m V_m / J_{sc} V_{oc}$$

The power efficiency of the cell is the ratio of the maximum electrical power density to the incident light power density $P_{in}$

$$\eta = J_m V_m / P_{in}$$

In addition to the above mentioned figures of merit, the monochromatic quantum efficiency of a device will be mentioned throughout this work. The external quantum efficiency (EQE) of a device is the number of electrons extracted divide by the number of incident photons at short circuit conditions; and the internal quantum efficiency (IQE) is the ratio of the number of electrons extracted to the number of photons absorbed, thus ignoring all optical losses.

Power is also dissipated through parasitic resistances ($R_S$ and $R_{SH}$). The equivalent circuit of a solar cell is depicted in Figure 2.2. The parasitic shunt resistance

($R_{SH}$) will be discussed further in chapter 4 in relevance to the fabricated photovoltaic devices [6].

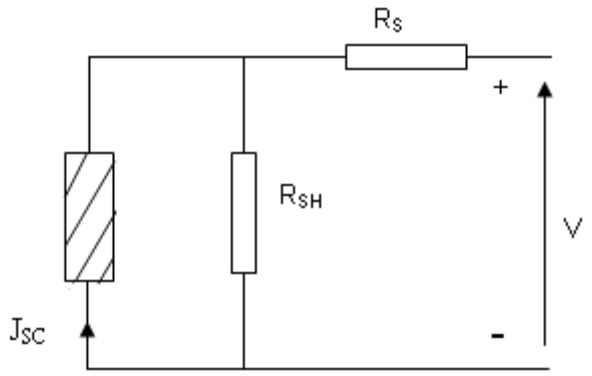


**Figure 2-2 Equivalent circuit of a solar cell**

From the figures of merit already cited, we can ascertain the properties of an efficient solar cell. Clearly, an efficient solar cell will have to have a high short circuit current, a high open circuit voltage and a fill factor close to unity. Specifically, the solar cell must be designed for minimum recombination losses throughout the device, and maximum photon absorption [4]. Solution-processed photovoltaics will be the focus of discussion in the following sections.

## 2.2 Conjugated Polymers

During the past 30 years, organic conjugated polymers have been investigated for a range of semiconductor devices such as transistors [19,20], photodiodes and photovoltaics [21], and light emitting diodes [22,23]. The prospect of low-cost production has propelled organic photovoltaic research. Conjugated polymers combine the low-cost,

high production-yield processability and the mechanical flexibility of conventional plastics with the chemically tailored electronic features of organic semiconductors [24].

### 2.2.1 Properties

Semiconducting organic materials are able to transport electric current and absorb light in the ultraviolet-visible part of the solar spectrum [25]. The energy gap between the top of the π-band (highest occupied molecular orbital, HOMO) and the bottom of the π*-band (lowest unoccupied molecular orbital, LUMO) is typically between 1.5 and 2.5 eV. Absorption of a photon of the visible part of the electromagnetic radiation promotes an electron from the completely filled π-band to the π*-band. The absorption spectrum of conjugated polymers therefore can be tuned to match well-defined portions of the solar spectrum [24].

An important difference to inorganic solid-state semiconductors lies in the generally poor charge-carrier mobility in these materials. They also have small exciton diffusion lengths. These combined features of organic semiconducting materials generally lead to devices with very small layer thicknesses (< 100 nm) [25].

### 2.2.2 Device Architectures

The first organic photovoltaic solar cells were based on single organic layers sandwiched between two metal electrodes. The rectifying behavior of single layer devices was attributed to the formation of a Schottky-barrier between the p-type hole conducting organic layer and the metal with the lower work function. Under AM1.5 conditions, the power conversion efficiencies recorded for this architecture were less than a unity [25].

The failure of this design was attributed to the high exciton binding energy in organic semiconductors where the built-in electric fields are usually not high enough to dissociate the excitons. Furthermore, due to the small exciton diffusion length for organic solar cell materials, excitons in the active layer had high probability of recombining before extraction [25].

The bilayer heterojunction concept was later introduced [26] where two organic layers with specific electron or hole transporting properties were sandwiched between a transparent conducting oxide and a semitransparent metal electrode. In this architecture, the electron is transferred from a p-type hole conducting polymer onto an n-type electron conducting $C_{60}$ molecule; the notation of donor (D) and acceptor (A) with respect to the electron transfer was introduced [25]. The maximum open circuit voltage is given by the maximum splitting of the electrochemical energy of the electron–hole pair under illumination, corresponding to the difference between the LUMO level of the acceptor and the HOMO of the electron donor [24].

In a bilayer device, a donor and an acceptor material are stacked together with a planar interface. The charge separation is facilitated by the large potential drop between donor and acceptor. The bilayer is sandwiched between two electrodes matching the donor HOMO and the acceptor LUMO, for efficient extraction of the corresponding charge carriers.

Within these devices, after exciton dissociation at the D/A interface, the electrons travel within the n-type acceptor, and the holes travel within the p-type donor material (Figure 2.3 (a)). Hence, holes and electrons are effectively separated from each other, and charge recombination is greatly minimized [25, 27]. A power conversion efficiency of

4.4% has been achieved by using poly(3-hexylthiophene) (P3HT)/ phenyl-C61-butyric acid methyl ester (PCBM) as D/A layers and the inclusion of poly(3,4-ethylenedioxythiophene) poly(styrenesulfonate) (PEDOT:PSS) as an electron blocking layer [25].

A further improvement is obtained by blending two polymers having donor (D) and acceptor (A) properties in solution; a bulk heterojunction of large interfacial area throughout the active region is formed. Thus, each donor–acceptor dissociating center is within a distance less than the exciton diffusion length of each absorbing site; ideally all excitons are dissociated within their lifetime. The charges are also separated within the different phases, and hence recombination is also minimized (Figure 2.3 (b)) [25,27].

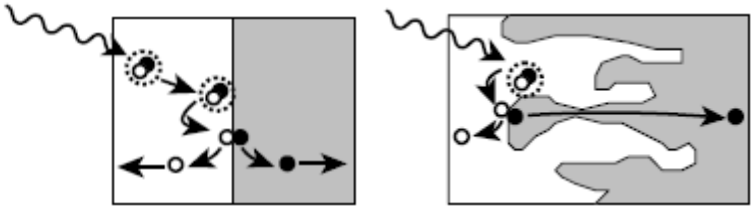

**(a)** **(b)**

**Figure 2-3 Diagrams of type of donor-acceptor organic photovoltaic cells (a) bilayer and (b) bulk heterojunctions [27].**

The bulk heterojunction is sensitive to the nanoscale morphology in the blend because it requires continuous pathways for the hole and electron all the way to their respective contacts [25]. A bulk heterojunction polymer based solar cell recorded an efficiency of 6.1% under AM1.5 illumination. The device was formed from a blend of P3HT and PCBM with PEDOT:PSS film functioning as an electron blocking layer [7].

More recently, efforts to utilize a larger fraction of the solar spectrum have been reported; a tandem solar cell where two bulk heterojunctions were superimposed

recorded an efficiency of 6.5% [28]. All constituents of this device were solution-processed thus minimizing the complexity of the fabrication process.

### 2.2.3 Limitations

Organic solar cells are being investigated as viable alternatives to conventional ones; they offer the prospect of using cheaper and flexible processing as opposed to complicated and restrictive ones. However, researchers have encountered many limitations preventing the achievement of higher performance.

In addition to their poor electrical properties embedded in their low mobilities and small exciton diffusion length, stability is a major factor hindering their progress. Conjugated polymers must be isolated from air and moisture to retain their efficiencies over time. Encapsulation techniques as applied to organic light-emitting diodes [29] have been proposed to protect the active materials from oxidizing agents.

Another impediment in the organic solar cell research is their inability to harvest all regions of the solar spectrum. Currently available conjugated polymers can only be tuned to match defined portions of the solar spectrum; as depicted in Figure 2.4, their absorption onset tend to only cover the ultraviolet-visible range [25]. However, half of the sun's power lies in the infrared. As a result, the optimal bandgap in single-junction solar cell lies at 1100 nm conveniently matching the absorption onset of silicon.

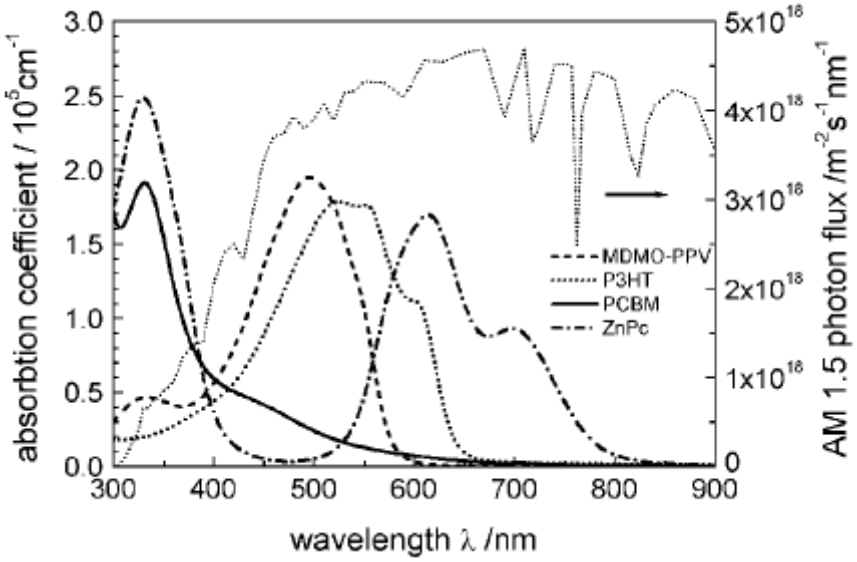


**Figure 2-4** **Absorption coefficients of films of commonly used materials are depicted in comparison with the standard AM 1.5 terrestrial solar spectrum [25].**

Furthermore, attempts to extend organic solar cell efficiency into the near infrared have so far pushed the absorption onset only to 1000 nm [30]. Therefore the greater portion of the near infrared region remains unexploited by conjugated polymers; there is an urgent need for a new solution-processed infrared sensitive material system. Lead salt colloidal quantum dots are viable candidates and have shown promise.

## 2.3 Semiconducting Nanocrystals

One of the primary motivations for studying nanometer-scale semiconductor crystallites or simply nanocrystals is to understand what properties are affected when the material becomes of nano-scale dimensions. Over the past decades, various types of nanocrystals have been studied and different shapes have been explored. Nanocrystals often retain the properties of their bulk counterparts while allowing simple spectral

tailoring. The following theoretical considerations must be reviewed to understand the basic fundamentals of the active material of the photovoltaic devices reported herein.

### 2.3.1 Properties

An important parameter of a semiconductor material is the value of the energy gap that separates the conduction energy band from the valence band. In macro-scale semiconductors, the width of the band gap is fixed and determined by the nature of the material. The situation is quite different in the case of nanoscale semiconductor particles; in the regime of quantum confinement, the continuous energy bands of the bulk material collapse into discrete energy levels (figure 2.5). The electronic excitations become deeply affected by the particle boundaries and tunable by varying the particle's size. Accordingly, as the quantum dot size decreases, the energy gap increases leading to a blue shift in the emission spectrum [31]. Through careful and simple adjustments of the synthesis conditions, the semiconductor nanocrystals allow easy access to the different portions of the solar spectrum, ranging from the visible to the near-infrared. The first observations of the described size dependence of the optical properties of quantum dots in II-VI and III-V materials were reported in the early 1980's by Efros, [32] Ekimov [33], Brus [34] and Henglein [35].

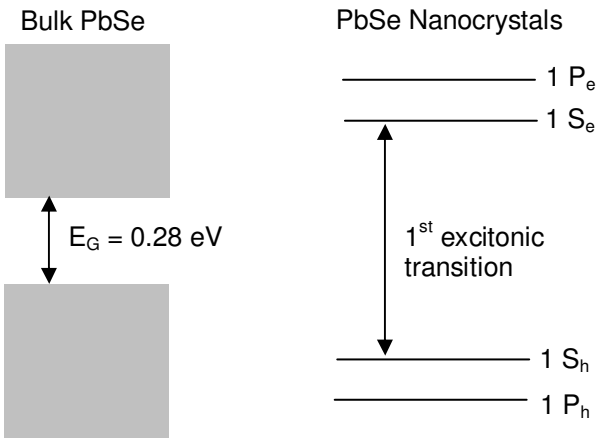


**Figure 2-5 continuous energy bands in bulk PbSe (left), discrete energy levels in PbSe nanocrystals (right)**

When a direct-gap semiconductor absorbs a photon, an electron is excited from the valence band into the conduction band. When moving to the quantum confinement regime, the size of the nanoparticle structure becomes comparable to the size of carrier's wavefunction; the carriers become confined by the boundaries of the material.

As a convenient scale, we define the Bohr radius of a particle as

$$a_B = \varepsilon \frac{m}{m^*} a_0$$

where $\varepsilon$ is the dielectric constant, $m^*$ is the effective mass of the particle, $m$ is the rest mass of the electron, and $a_0$ is the Bohr radius of the hydrogen atom. We consider three different Bohr radii: one for the electron ($a_e$), one for the hole ($a_h$), and one for the electron-hole pair ($a_{eh}$), sometimes refer to as exciton. The latter is bound by Coulombic attraction forces. In the strong confinement regime, the nanocrystal radius $a$ is much smaller than $a_e$, $a_h$, and $a_{eh}$ , and the carriers are strongly confined to the boundaries of the quantum dot [31,36].

We will consider the properties of electron-hole pair states resulting from the effective mass approximation model. We will treat a crystallite that has a large number of

atoms as a quantum box for carriers. The particle-in-a sphere model provides a quantitative description of the size dependent electronic properties of a quantum dot [34]. Starting with a particle of mass $m_0$ inside a spherical potential well of radius $a$, the Shrodinger's equation yields the following expression for the particle's energy

$$E_{n,l} = \frac{\hbar^2 k_{n,l}^2}{2m_0} = \frac{\hbar^2 \alpha_{n,l}^2}{2m_0 a^2}$$

where $\alpha_{n,l}^2$ is the n$^{th}$ order zero of the l$^{th}$ order spherical Bessel function, and $\hbar$ is Plank's constant. In real time situations, the nanocrystals are not actually confined alone in a sphere [31,36]. The above equation demonstrates the inverse square relationship between the energy gap and nanocrystal radius.

### 2.3.2 Lead Salt Quantum Dots

Lead salt quantum dots, unlike other materials, offer easy access to the regime of extreme quantum confinement. Their large carrier Bohr radii (23 nm) allow strong confinement to be achieved in larger structures. They have small electron and hole masses which translate into large confinement energies, split equally between the carriers. As a result, lead salt quantum dots have simple electronic spectra where the conduction and valence energies shift by the same amount from their bulk values (refer to Figure 2.5) [37].

The quantum confined lead salt colloidal quantum dots can be engineered to access the visible and the short-wavelength infrared spectral regions via simple variation the chemical synthesis. The minimum transition energy for PbS and PbSe QDs is given by their bulk bandgap, 0.41 eV and 0.28 eV respectively [38]. Consequently, PbSe quantum

dots have the potential of reaching further deep into the mid-IR range which is inaccessible by conventional bulk semiconductors and conjugated polymers [37]. In order to take advantage of the Sargent group's extensive expertise with the PbS nanocrysatls, PbSe nanocrysatls reported in this work were synthesized using a modified version of the organometallic route used for PbS nanocrysatls synthesis. We will present a brief overview of recent attempts to fabricate infrared-sensitive photovoltaic devices.

### 2.3.3 IR Quantum Dot Photovoltaics

Nanocrystals have been extensively used over the past decade side by side with polymers because they behave as good electron acceptors and they allow spectral tunability through simple chemical variations. Most reports focused on cadium chalcogenide nanocrystals which absorb in the visible range. In 2005, Gur *et al.* reported the best all inorganic nanocrystal solar cell with an AM1.5 power conversion efficiency reaching 3%. Again, the later device failed to harvest light beyond 850 nm [8]. Other notable work on visible nanocrystals was carried out by Greenham [39,40], Alivisatos [41,42], and Bawendi [43].

Recently, organic polymers sensitized using infrared lead salt nanocrystals have been investigated; however, these devices did not exceed monochromatic power conversion efficiencies of 0.1% [11, 17, 18, 44, 45]. The active layer consisted of either a blend of a polymer with PbS nanocrystals or a bilayer heterojunction between the two materials; the nanocrystal active layer in both architectures was used as an electron acceptor layer in a D/A configuration. In 2007, Klem *et al.* reported 1.3% monochromatic infrared power conversion efficiencies in an all-inorganic PbS nanocrystals based device

through the use of thiols and high temperature processes to achieve smooth films on rough nanoporous transparent metal oxides [14]. More recently, the highest infrared monochromatic external quantum efficiency (EQE) yet achieved with nanocrystals was reported: 37% under 12 mW $cm^{-2}$ illumination at 975 nm [15]. These PbS colloidal quantum dot based devices registered an infrared power conversion efficiency of 4.2%.

In regards to PbSe nanocrystal based PV device, relatively low efficiencies have been reported; devices based on polymer/PbSe nanocrystal blend recorded AM1.5 power conversion efficiency of only 0.04% [18]. A similar architecture was used by Cui *et al.* who obtained 0.14% power conversion efficiency under AM1.5 illumination [17]. Herein, we thought to investigate an all-inorganic PbSe nanocrystal based device structure without the inclusion of conjugated polymers. A Schottky barrier is thus formed between the active infrared-sensitive device and the low work function metal contact.

## 2.4 The Schottky Barrier

A Shottky barrier can form when a doped semiconductor is contacted with a metal [6]. The metal-semiconductor diode was one of the first semiconductor based devices used in the 1900s. It was made by contacting a metallic whisker to an exposed semiconductor surface [46]. Understanding the concepts underlining its operation came later with pioneering work by Schottky, Stormer and Waibel. The following section will give an overview of the Schottky junction fundamentals ignoring non-ideal surface effects. We will also describe a successful attempt at Schottky-quantum dot photovoltaics done by the Sargent group.

### 2.4.1 Concepts

When a p-type doped semiconductor of work function $\phi_p$ and a metal contact of work function $\phi_m$ , such that $\phi_p > \phi_m$, are isolated from each other, their respective Fermi levels are as depicted in Figure 2.6 (left). At contact, the Fermi levels line up and the vacuum level changes by $(\phi_p - \phi_m)$ between the semiconductor and the metal.

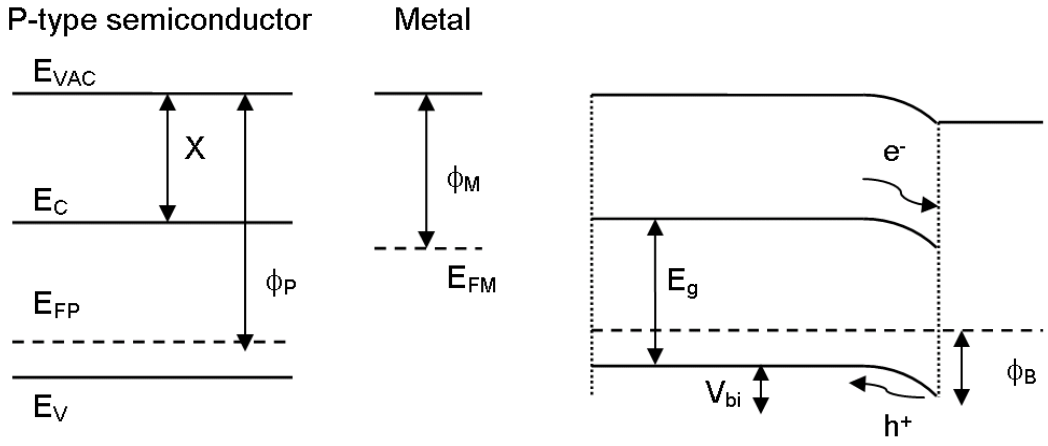


**Figure 2-6 (left) energy-band diagram of a metal and a p-type semiconductor before contact (right) after contact a Schottky barrier is formed.**

Practically, carrier redistribution across the interface occurs until thermal equilibrium is reached: a space charge region is created. The energy at the valence band edge in the bulk of the semiconductor is effectively higher than at the interface with the metal; the semiconductor bands bend and a built-in field is established. The parameter $\phi_B$ is the barrier height seen by the holes in the metal trying to move into the semiconductor. It is the Schottky barrier and is given by

$$\phi_B = (\chi + E_g) - \phi_M$$

where $\chi$ is the electron affinity of the semiconductor as indicated in Figure 2.6.

The total amount of band bending in the semiconductor is the barrier seen by the holes in the semiconductor trying to flow into the metal and is given by $qV_{bi}$ where $V_{bi}$ is the built-in bias. It is expressed as the difference between the Fermi energies of the isolated metal and the semiconductor

$$V_{bi} = E_{FM}-E_{FP}$$

The space charge region formed at thermal equilibrium is depleted from carriers and is often called the depletion region. The electric field set up in the depletion region will drive the charge separation mechanism. In the presence of illumination, the holes will be accumulated in the p-type semiconductor and the electrons in the metal after successful carrier separation. The electron-hole pairs that are generated deep in the active layer diffuse towards the depletion region before getting separated and extracted [6,46].

In the case where the metal work function is higher than that of the p-type semiconductor, an ohmic contact is formed; the transport of majority carriers across the junction is facilitated by the resulting band bending and the flow of minority carriers is inhibited. Majority carriers accumulate near the interface and thus the current flows easily in both directions [46].

Practically, non-ideal density states are present at the surface of the semiconductor; they result from dangling bonds and existent impurities. In actuality, the electronic properties of the surface of the semiconductor often differ from the bulk properties. Thus, the metal-semiconductor junction rarely behaves as described above. In the presence of a large amount of surface states, the Fermi energy level can easily be pinned regardless of the nature of the metal contact [6].

### 2.4.2 PbS nanocrystal Schottky barrier

In 2007, Clifford et al. reported a detailed analysis on the formation of a Schottky barrier between lead salt colloidal quantum dots and a metal contact [47]. More recently, Jonhston et al demonstrated efficient infrared energy conversion efficiency using a PbS nanocrystal Schottky barrier photovoltaic device. The amine-capped PbS nanocrystals were spin-coated on top of a thin layer of indium tin oxide (ITO). The Al low work function metal contact was thermally deposited. The PbS nanocrystal film behaved as a p-type semiconductor layer and thus formed a Shottky junction when contacted with Al. They reported an external quantum efficiency of 37% and an infrared power conversion efficiency of 4.2% under under 12 mW $cm^{-2}$ illumination at 975 nm. Furthermore, carrier drift through the depletion region near the Schottky contact was determined to be the dominant transport mechanism. However, these devices did not retain their high efficiencies for a long period of time and the contacts we found to be prone to degradation [15,48].

## 2.5 Strategy

We set out to fabricate high efficient solution processed infrared sensitive devices that could potentially be included in a tandem cell. PbSe nanocrystals have been reported in literature as having high carrier mobilities [49] and have been previously used as the active layer of photovoltaic devices [17, 18]. We selected PbSe nanocrystals because we wanted to explore the possibilities this new material system could offer us. The synthesis process was optimized to produce stable semiconducting material for efficient infrared

sensitive solar cells. The optimal goal of these devices is their inclusion in the multijunction device architecture as previously mentioned. Thus, the infrared single junction solar cells should be optimized for infrared power conversion efficiency rather than solar power conversion efficiency. Herein we report the first PbSe colloidal quantum photovoltaic to exceed one percent infrared power conversion efficiency. It also represents the first solution-processed infrared photovoltaic device to be stable over weeks without requiring fresh deposition of its top electrical contact.

To achieve this record combination of efficiency and stability, we developed and pursued a materials processing strategy as follows:

- we believed that nanocrystal-capping ligands such as butylamine, while short in length and thus consistent with reasonable carrier transport, are sufficiently labile as to imperil the stable passivation of thin solid films over days and weeks. We therefore selected a more strongly-binding end functional group to passivate our nanoparticle surfaces robustly in the solid state.
- we believed that further increase in proximity among the nanoparticles could be achieved, and could result in improved electron and hole transport, without sacrificing the highly desired quantum size-effect tuning offered by the use of colloidal quantum dots. We therefore pursued a short bidentate linker having a conjugated, instead of an entirely insulating, moiety lying between the end groups.
- finally, we were concerned that too large a change in film volume resulting from the exchange of longer oleic-acid-capped ligands to short crosslinkers would lead

to poor film morphology and electrical shorts. We pursued therefore solution-exchange to a shorter linker prior to film formation and film crosslinking.

These considerations, taken together, led us to first use a solution-phase exchange to an intermediate ligand, octylamine; followed by solution-casting of films; and finished with a treatment using the bidentate linker, benzenedithiol. The material and device processing will be detailed in the following chapters.

# 3 PbSe Nanocrystals

The last chapter positioned our work within the context of the state of the art solution processed photovoltaics. It also served as an overview of the fundamentals that we will be using throughout our discussion. The following chapter focuses on the chemical processing of the PbSe nanocrystals in solution form. PbSe nanocrystals had never been used within the Sargent group; thus, there was no prior experience on its synthesis and processing. We needed to develop the material from scratch and optimize it for efficient photovoltaic devices. We were successful in establishing a reliable synthesis process followed by a solution-based ligand exchange aimed at reducing the inter-nanoparticle distance for improved electrical properties.

## 3.1 Initial Observations

Bulk lead salts have been previously reported to be particularly sensitive to oxygen content [50, 51]; it was established that adsorbed oxygen on lead salt surfaces plays an important role in their photoconductive response [50]. Inherent of their colloidal nature, semiconductor nanocrystals have large surface areas and thus are prone to be sensitive to surface influences. Previous reports have revealed that the transport properties of nanocrystals are greatly hindered by surface dangling bonds [49, 52]. Recently, it was established that oxidation plays an important role in affecting the performance of PbS [53] and PbSe nanocrystal based devices [54]. Herein, we report the first attempt of the Sargent group to synthesize stable colloidal PbSe nanocrystals using a convenient analogue version of the organometallic route previously reported for PbS nanocrystals

[55]. In literature, a different synthetic route is usually reported for PbSe nanocrystals [56]. Using the materials and expertise at our disposal, we had to develop our own processing strategy to yield stable colloidal PbSe nanocrystals.

Following the exact synthesis process of PbS nanocrystals, we were not successful in attaining stable well dispersed PbSe nanocrystals in solution. They seemed to be highly reactive to oxygen and often formed agglomerates within a day of synthesis, unlike their PbS counterparts. We had to completely isolate the nanocrystals in their solution form from oxygen. We divided the synthesis process into two stages; the first one performed by Dr. Larissa Levina was done under constant flow of Argon in a Schlenk line; the second stage involved isolating the nanocrystals from the reaction mixture and was performed in a nitrogen-filled glovebox. Figure 3.1 shows transmission electron microscopy of PbSe nanocrystals stored in air versus ones isolated in the glovebox.

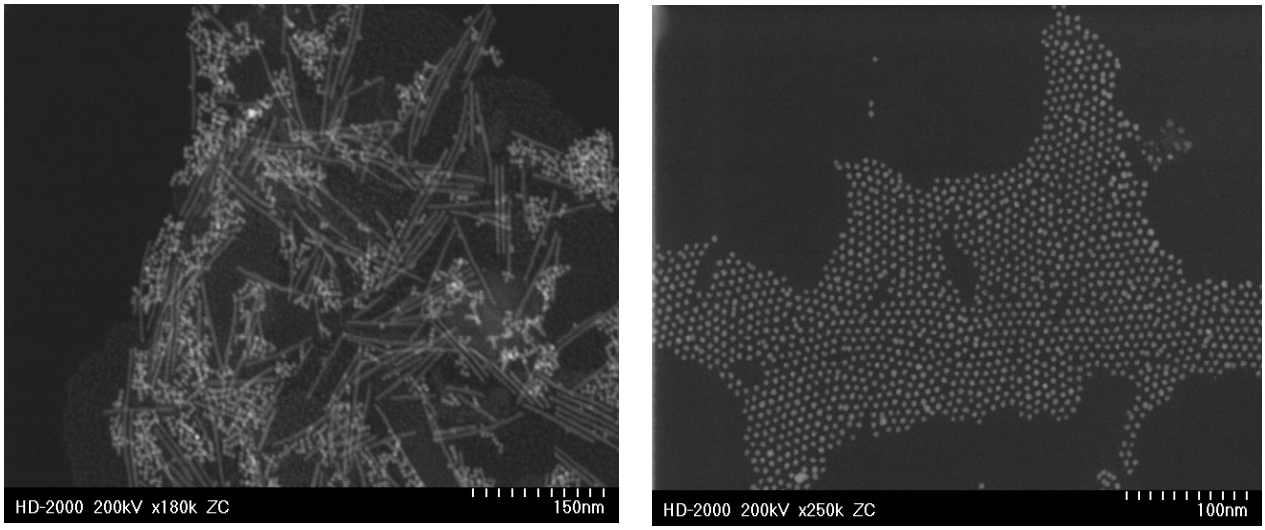


**Figure 3-1 PbSe nanocrystals exposed to air (left), and isolated in inert atmosphere (right)**

## 3.2 Chemical Synthesis

In the following section the chemical synthesis of colloidal semiconductor nanocrystals will be described. We will then detail the procedure followed to fabricate the PbSe nanocrystals used in this work. Semiconductor nanocrystals have been prepared by a variety of methods, such as molecular-beam-epitaxy, and metalorganic-chemical-vapor-deposition. Here, we emphasize the colloidal chemical synthesis of crystalline semiconductor nanoparticles.

### 3.2.1 General Description

A successful nanocrystal preparation is usually based on the decomposition of metal-organic precursors in hot coordinating solvents (120-360$^{o}$C). Referring to the pioneering work of La Mer and Dinegar on colloidal particle nucleation and growth [57, 58], the synthesis involves a discrete nucleation event followed by rapid growth from monomers and finally slower aging process, called Ostwald ripening. The precursor is first rapidly injected into the hot coordinating solvents which triggers nucleation. As a result, the reagents are decomposed and supersaturation of the monomersis achieved. As long as the monomers are added, particle growth continues. During the final slow aging process, smaller particles dissolve into larger particles for improved monodispersity [31].

Alternatively, slow ramping of the reaction temperature can trigger supersaturation and nucleation. Accordingly, precursors are mixed at low temperature and slowly brought to the desired temperature at which decomposition occurs. Supersaturation is again followed by particle generation and growth [31].

The final stage involves washing the nanocrystals and isolating them from the rest of the reagents. A non-solvent is added to the final mixture and the nanocrystals are precipitated; the supernatant containing the by-products is discarded. The washed nanocrystals are then redispersed in the desired nonpolar solvent.

The major advantage of the colloidal nanoparticle synthesis is the ability to tailor the absorption spectrum, i.e. control the size of the particle, through simple variation of the chemical process. Size and size dispersion can easily be controlled using different reaction times, nucleation and growth temperatures, precursor concentrations, stabilizer/precursor ratios and capping ligands [31]. Figure 3.2 depicts the absorption spectra of different sizes of PbS nanocrystals [55].

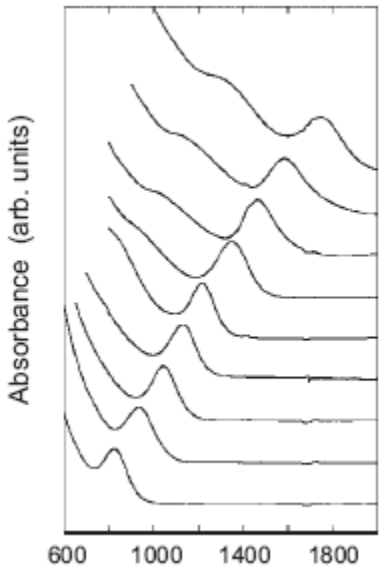


**Figure 3-2 Absorption spectra of PbS nanocrystals of different sizes[55].**

PbSe colloidal nanocrystals are usually synthesized from lead oleate and trioctylphosphine selenide (TOPSe) [56]. We chose another alternative approach. The

next section will describe the detailed chemical synthesis of the PbSe nanocrystals used herein.

### 3.2.2 Procedure

As previously mentioned, we took advantage of the Sargent group expertise and synthesized PbSe nanocrystals using the analogue version of the organometallic route previously reported for PbS nanocrystals [55]. The following is the complete recipe to produce the nanocrystals used in the reported high efficiency photovoltaic devices.

The non-coordinating solvent octadecene (ODE) was first degassed by pre-pumping at 80$^{o}$C for 16 hours and the Bis(trimethylsilyl)selenide (TMSe) precursor was pre-filtered with 0.1 and 0.02 μm polytetrafluoroethylene filters before use. The synthesis was performed in a single, three-neck, round bottom flask. The Pb precursor was prepared by pumping the mixture of lead oxide (PbO) powder and oleic acid (OA) at 80$^{o}$C for 16 hours. The resulting transparent solution of lead oleate precursor was stirred vigorously while being heated under Ar for about 30 min. The stock solution of selenium precursor was prepared by mixing TMSe with ODE in a glovebox and the portion corresponding to a 2:1 (Pb:Se) molar ratio was rapidly injected into the reaction flask. The injection temperature ranged between 125$^{o}$C for smaller nanocrystals and 140$^{o}$C for the largest NCs. Upon injection, nucleation occurs instantly; thus, rapid injection is critical to achieve a narrow size distribution. After injection, the temperature of the reaction was dropped down and the reaction was quenched by subjecting it to a water-ice bath for 1 min and 40 sec. A typical synthesis for nanocrystals having their excitonic peak ranging from 1200 nm and 1300 nm involved injecting of 7 mL of selenium stock

solution (1 mmol of TMSe) into the reaction flask containing 2 mmol PbO (0.45 g), and 63 mmol of OA. The synthesis process up to this point was performed by Dr. Larissa Levina; we performed all the remaining chemical and device processing reported in this thesis.

As previously mentioned, PbSe nanocrystals, particularly in their solution phase, were observed to be extremely sensitive to ambient conditions and as a result all post-synthetic treatments were performed in a glove box with anhydrous reagents. The oleate-capped PbSe nanocrystals were isolated from any remaining starting materials and side products by precipitating the solution with a mixture of equal volumes of methanol (5 mL) and ethylacetate (5 mL). The precipitate was then re-dispersed in toluene and re-precipitated with methanol. After the second precipitation, the nanocrystals were vacuum-dried for 10 min and redispersed in toluene. For this particular synthesis, it was unnecessary and even disadvantageous at times to expose the nanocrystals to further aging, which stands in contrast with the synthesis for PbS nanocrystals [55].

## 3.3 Solution Ligand Exchange

### 3.3.1 General Description

As-synthesized colloidal nanocrystals comprise an inorganic core usually surrounded with a layer of organic capping ligand molecules. Generally, the latter provide surface passivation and allow the nanocrsytals to be stably suspended in solution, thus preventing agglomerations [56].

A solution ligand exchange is the chemical process by which the original capping groups prone to detach from the nanocrystals surface are exchanged with other

competing, usually shorter, capping ligands. The latter process can be achieved either by immersing the nanocrystals in an excess of another weak ligand or a small amount of strongly bound ligand. After a controlled duration, the nanocrystals are precipitated by adding a non-solvent to the mixture and then redispersing the exchanged nanocrystals in the final solvent. This process allows the adjustment of the length and chemical functionality of the organic capping layer and hence the use of the nanocrystals in various applications [56].

The as-synthesized PbSe nanocrystals are initially capped with oleate ligands (~2 nm) previously reported to impede efficient charge transport in films. Exchanging the oleate ligands to shorter amines such as octylamine (~1 nm) and butylamine (~0.6 nm) has been shown to produce a closer packed nanocrystal film and improve electrical properties [11, 12,13, 14, 15]. The following section will focus on the process developed to exchange the long native ligands to shorter ones.

### 3.3.2 Procedure

We initially tried to exchange the PbSe nanocrystals using the developed processing strategy used for PbS nanocrystals by which oleate ligands are replaced to a large extent by butylamine ligands [14, 15]. However, working with the four carbon chain amine proved to be very difficult and unreliable, yielding unstable final solutions. The reaction times, the amount of non-solvents used at each processing step, the duration of the drying process, the final solvent used seemed to be batch to batch dependent. We later investigated and optimized the exchange of the oleate ligands to octylamine. We

were successful in establishing a reliable repeatable process. The following describes the optimal solution exchange process of the PbSe nanocrystals.

The solution exchange procedure was carried out inside a nitrogen filled glovebox. The as-synthesised nanocrystals (Figure 3.3 (a)) were precipitated with methanol, vacuum-dried for 10 min, and redispersed in octylamine. After three days, we precipitated the nanocrystals with anhydrous isopropanol, vacuum-dried them for 10 min and redispersed them in octane solution to achieve a typical concentration of 80 mg $mL^{-1}$.

PbSe nanocrystals having an absorption peak ranging between 1200 and 1300 nm before and after solution exchange (Figure 3.3 (a) and (b)) were used to fabricate the photovoltaic devices .


**(a)**

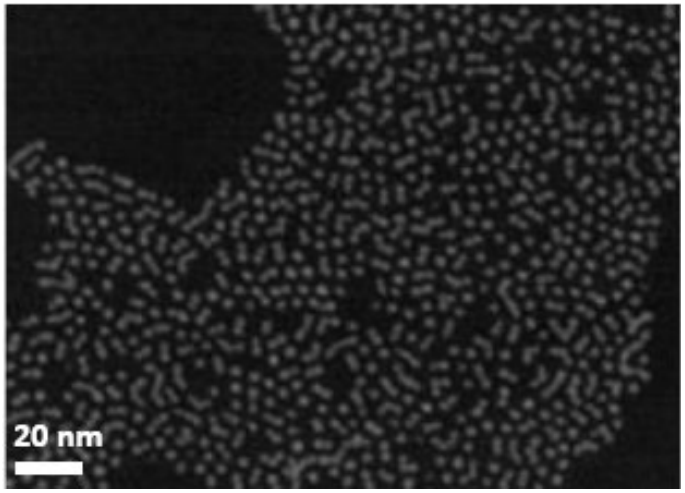


**(b)**

**Figure 3-3 Transmission Electron Microscopy of PbSe nanocrystals. A) as-synthesized oleic-acid capped PbSe nanocrystals used in this investigation (~ 5 nm in diameter) B) after octylamine ligand exchange the inter-nanoparticle distance was reduced.**

## 3.4 Conclusion

This chapter aimed to describe the chemical synthesis of the PbSe nanocrystals used in this work. The literature reports and our own results can be summarized as follows:

- The advantage of using colloidal nanocrystals lies in the ability to tailor their size through simple and controllable variations to the reaction parameters.
- PbSe nanocrystals in solution were observed to be dramatically unstable when exposed to ambient conditions and thus necessitated complete isolation in a nitrogen filled glovebox.
- Following an optimized processing strategy, a reliable and repeatable synthesis of PbSe nanocrystals was developed in the Sargent group.
- Long native capping ligands impede film transport properties and thus a successful exchange to a shorter amine ligand was developed.

It is important to note that the nanocrystals while still in solution were isolated at all times from oxygen. The next chapter will be dedicated to describe the film deposition process and the crosslinking solid state treatment that proved to be essential for high efficiency device fabrication.

# 4 Device Fabrication

The previous chapter presented the chemical processing of the PbSe nanocrystals. It was noted that the nanocrystals in solution were highly reactive to oxygen and thus required completely air-free processing. In the present chapter, we will describe the deposition process of the nanocrystal films and the solid state processing that proved to be necessary to obtain efficient photovoltaic devices. We note here that all measurements throughout this work were done in air.

## 4.1 Film Deposition

The octylamine capped PbSe nanocrystals were spincoated on top of a transparent contact oxide as a first step towards fabricating a photovoltaic device. The following section discusses the complications we faced, the strategy we pursued to overcome them, and the optimization process we developed to improve the efficiency of the photovoltaic devices.

### 4.1.1 Single Layer devices

The initial attempts were inspired from the fabrication process of the previously reported efficient PbS based devices [15]. Accordingly, we tried to deposit a single nanocrystal layer on top of indium tin oxide (ITO) and evaporate an aluminum contact on top. In our experience, these devices failed to produce any photovoltaic effect. Using ITO as a bottom transparent contact, we also evaporated different top contacts (Mg, In, Ag, Au) with varying work functions on the nanocrystals film but all failed to provide any

photovoltaic response as shown in Figure 4.1**.** Furthermore, we were not successful in fabricating devices with different bottom contacts (Au, Ag, Pt, Al).

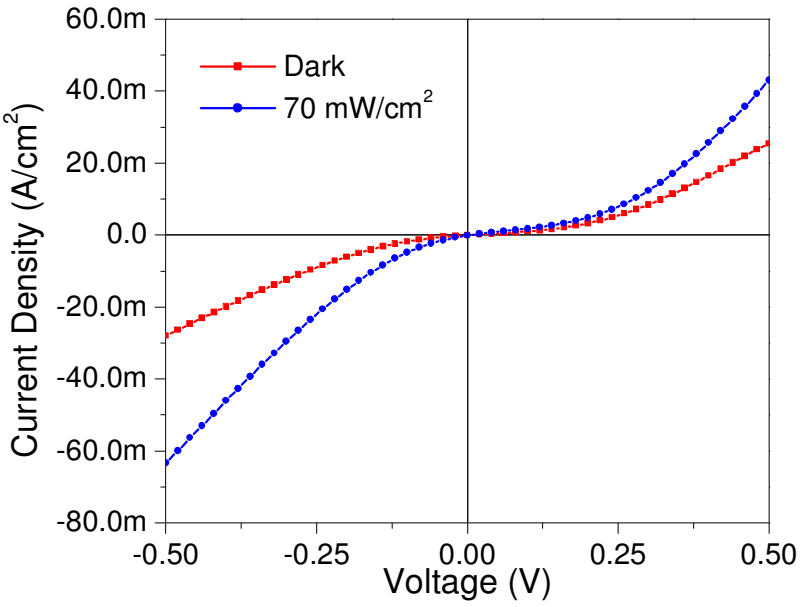


**Figure 4-1Symmetrical curves for PbSe nanocrystal based devices without any solid state treatment. Similar curves were obtained with Al, Mg, Ag, Au top contacts and ITO, Au, Ag, Pt bottom contacts**

Our failed attempts are in contrast with recent findings with record-setting PbS colloidal quantum dot devices [15]. We tentatively conclude that PbSe nanocrystals are particularly sensitive to the requirement of effective surface passivation. As a result, we pursued a more strongly-binding end functional group to passivate our nanoparticle surfaces robustly in the solid state.

### 4.1.2 Crosslinking Solid State Treatment

We speculated that the as-exchanged nanocrystals were dominated by a large density of unpassivated surface states. Colloidal nanocrystals have been widely reported

to be deeply affected by a large density of unpassivated surface states inherent to their large surface area. Various chemical treatments aimed at surface passivation have been reported on both PbSe and CdSe nanocrystals [52, 54, 59-63]. Herein, we selected a bidentate linker having thiol end groups that have a strong affinity to Pb atoms [14, 64], and that has been reported to facilitate charge transfer in nanocrystal solids [65].

The crosslinker solution was prepared by diluting 1,4-benzenedithiol (BDT) powder into a solution of acetonitrile (3.5 mM) and sonicating the mixture for 15 min.We spin-coated thin NC films (~110 nm) on ITO substrates and we immersed the samples in the benzenedithiol solution for a duration ranging from 10 to 30 minutes. This rendered the layer insoluble in the nonpolar solvents that were used for spin-coating the nanocrystals. We deposited a second thin layer on top to ensure the formation of a smooth, densely packed film. The second layer was also subjected to a linking treatment. The total thickness of the nanocrystals active layer ranged between 210 and 250 nm. Figure 4.2 (b) shows PbSe nanocrystals single- and double-layered films having an absorption peak ranging between 1200 and 1300 nm.

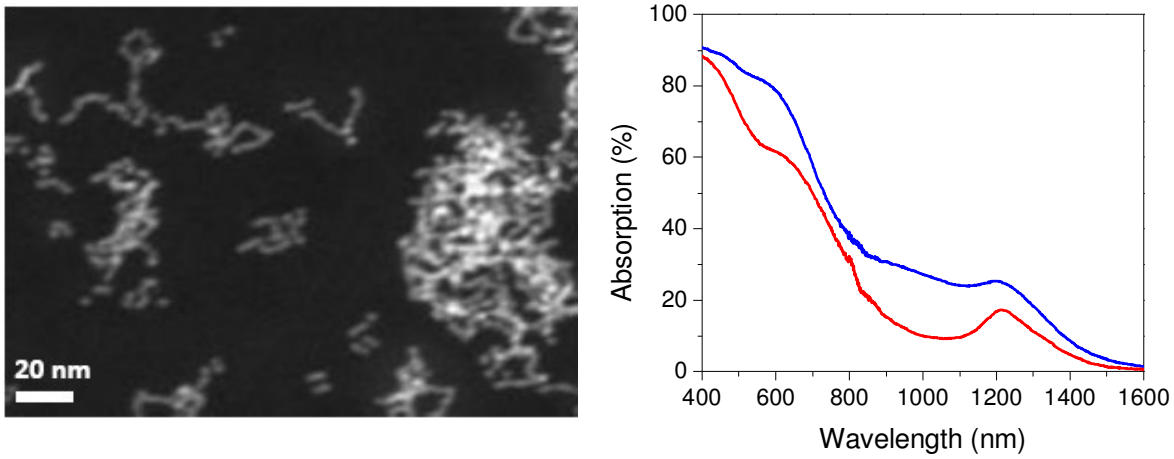


**Figure 4-2 (a) Transmission Electron Microscopy of PbSe nanocrystals after BDT treatment: formation of networks of nanocrystals due to the strong affinity of the thiol-end groups for the Pb atoms. (b) Absorption of single treated (red) and double treated (blue) layers.**

## 4.2 BDT treatment Optimization

As previously noted, PbSe nanocrystals have never been previously used within the Sargent group. With poor photovoltaic performances reported in literature [17,18], we had little expertise available to us; we had to develop chemical processes and optimize them from scratch. The present section will describe the strategy pursued to optimize the crosslinking treatment.

After exposing the nanocrystal layers to BDT, films were blown dry with nitrogen and subjected to 30 min vacuum drying. We further optimized our crosslinking treatment by varying its duration time for each of the two layers. Typically, we used 20 min treatment time for both layers; however, devices where the first layer was treated for shorter durations (~10 min) while the second one for longer (~30 min) recorded monochromatic power conversion efficiencies of exceeding 3% under 12 mW $cm^{-2}$ at

975 nm. The reduced treatment time for the first layer enabled us to realize smoother and defect-free films. The fill factor and the open circuit voltage both degraded when the first layer was subjected to more than 15 min treatment time. The latter fact correlates with the reduction of the shunt resistance of the device, i.e. pinholes due to the chemical processing increased. We show in Figure 4.3 the performance of three differently processed devices, two of which exhibited similar external quantum efficiencies. The device with 20 min treatment duration for both layers (Figure 4.3 -dashed red line) was deeply affected by processing defects because it exhibited the lowest open circuit voltage ($V_{oc}$) and fill factor. Optimization of the treatment duration was therefore essential to maximizing the performance while minimizing pinholes. Figure 4.3 also shows the best performance of an under-treated device (dotted black line) which had a better fill factor resulting from minimal defects but was not as efficient as our best passivated devices (solid blue line). Table 2 summarizes the figure of merits of differently processed devices recorded under 12 mW $cm^{-2}$ illumination at 975 nm.

**Table 1Effect of treatment duration. All the measurements were performed under 12 mW $cm^{-2}$ illumination at 975 nm**

| Treatment Duration (min, 1st layer:2nd layer) | $J_{sc}$(mA/$cm^2$) | $V_{oc}$(V) | FF (%) |
|---|---|---|---|
| 10:30 | 4.40 | 0.25 | 40 |
| 20:20 | 3.88 | 0.15 | 34 |
| 10:10 | 2.76 | 0.19 | 45 |

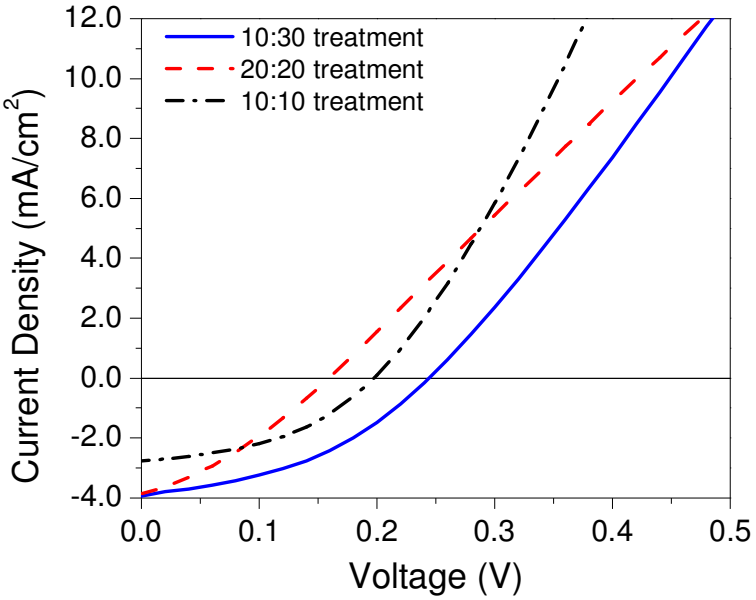


**Figure 4-3 Current-Voltage Characteristics of differently PbSe colloidal quantum dot treated devices. The best passivated device (blue) exhibit an IR PCE of 3.65% with 40% fill factor. The fill factor decreases to 34% when we increase the treatment duration of the first layer (red). The highest fill factor (45%) was registered for a reduced treatment time for both layers (black).**

## 4.3 Conclusion

We described in this chapter the detailed process to fabricate an efficient photovoltaic PbSe colloidal quantum dot device. The following summarizes the conclusions drawn from our experiments:

- Single layer devices processed as recently reported efficient PbS devices, where the active layer was not exposed to any post-fabrication treatment, did not yield any photovoltaic effect. We suspect that the PbSe nanocrystals are particularly sensitive to surface effects.

- As a result, we exposed the nanocrystal film to short bidentate linkers with thiol end groups that have strong affinity to Pb atoms. A second layer was added to ensure the formation of a densely packed film.
- The crosslinking treatment was further optimized to minimize defects and maximize device performance.

Once the device fabrication process was optimized, we characterized our devices' performance and electrical properties.

# 5 Device Characterization

As discussed in chapter 4, the benzenedithiol treatment was critical to yield efficient PbSe nanocrystal based photovoltaic devices. We present in this chapter the performance of the devices in terms of conversion efficiencies; spectral and intensity dependent external quantum efficiencies (EQE) are also reported. We report stable efficient infrared sensitive photovoltaic devices; all the chemical processes reported in the previous chapters have been optimized to yield the high performances. Furthermore, the strongly-bound dithiol group provided the needed passivation to drastically improve stability and played a key role in the observed photovoltaic performance. A stability study of these devices stored in both ambient and inert environment is presented. Finally, the carrier transport properties of the semiconductor films are evaluated; we find that the electron and hole mobilities are within the same order of magnitude in contrast with recent findings for PbS nanocrystals [48].

## 5.1 Photovoltaic Device Performance

We developed the first PbSe colloidal quantum photovoltaic to exceed one percent infrared power conversion efficiency (PCE) [17,18]. It also represents the first solution-processed infrared photovoltaic device to be stable over weeks without requiring fresh deposition of its top electrical contact.

### 5.1.1 Current-Voltage Characteristics

Figure 5.1 (a) shows our best recorded infrared power conversion efficiency of 3.6%. The EQE reached 46% under 12 mW $cm^{-2}$ illumination at 975 nm. The devices

exhibited a PCE of 1.1% under simulated solar illumination at 100 mW $cm^{-2}$ as shown in Figure 5.1 (b).

Our materials processing led to reproducibly high performance: throughout the course of this study, approximately 40 devices were made that exhibited infrared monochromatic power conversion efficiencies in excess of 3%.

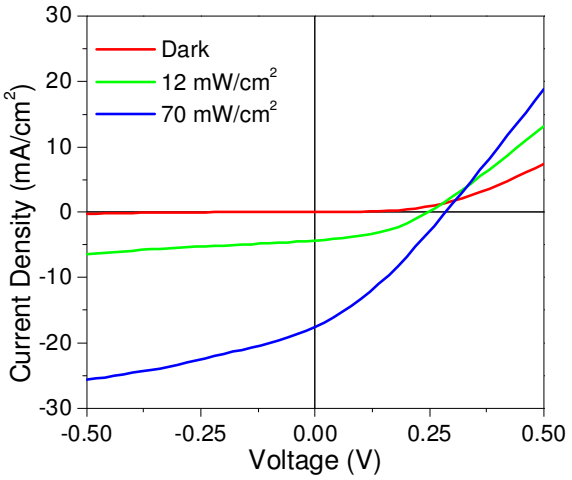


**(a)**

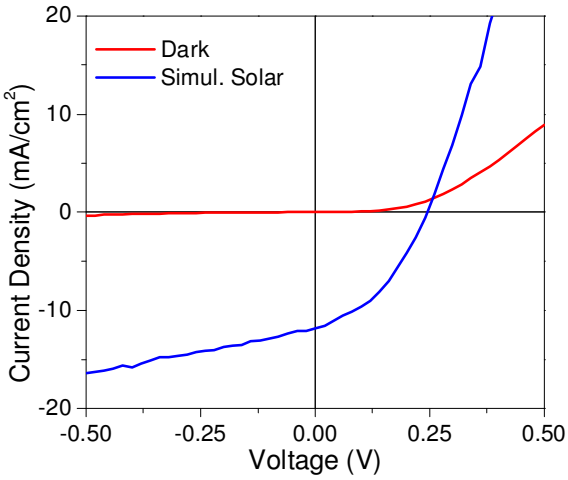


**(b)**

**Figure 5-1 Photovoltaic Device Performance. Current-voltage characteristics of a benzenedithiol treated two-layered device exhibiting A) 3.6% monochromatic power conversion efficiency at 975 nm under 12 mW $cm^{-2}$ illumination B) simulated solar power conversion efficiency of more than 1.1% (i.e. AM1.5 at 100 mW $cm^{-2}$).**

### 5.1.2 Spectral External Quantum Efficiency

We present the spectrally resolved EQE between 400 to 1600 nm in Figure 5.2. The EQE follows closely the features of the absorption spectrum shown in Figure 4.2 (b); a well-defined first excitonic peak is observable at 1250 nm. In the visible wavelengths, a peak EQE of 70% is recorded. From measurements of total film absorbance, we estimated the internal quantum efficiency at 975 nm to approach 90% in the best devices, which implies highly efficient charge separation and extraction. The roll-off at 500 nm is primarily due to increasing absorption in the ITO. Further details on the measurement procedure are presented in Appendix C.

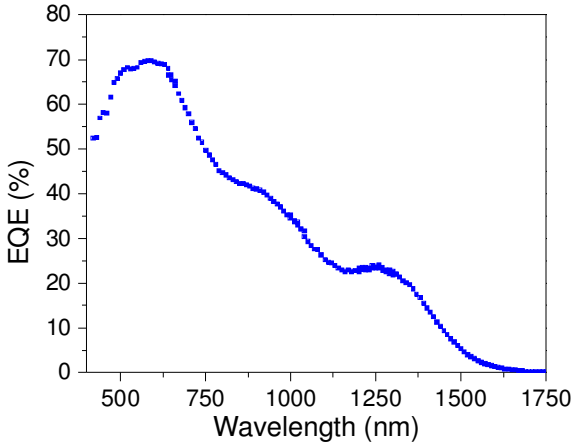


**Figure 5-2 Spectral external quantum efficiency of a device reaching 37% in the infrared and about 70% in the visible range. From total absorbance measurements at 975 nm, the IQE was found to approach 90%.**

## 5.2 Stability Study

The stability study for devices stored both in air and in nitrogen is summarized in Figure 5.3. When stored in a nitrogen-filled glove box for over two weeks, devices retained more than 75% of their initial high EQEs. We compare the stability of the devices fabricated in the present work with previously reported high-efficiency devices [15], fabricated as described by spin-coating butylamine-capped PbS nanocrystals on ITO

substrates and evaporating Al contacts on top [15]. The benzenedithiol-crosslinked PbSe nanocrystal devices retained their high EQEs over 10 days when stored under nitrogen, while the amine-capped devices lost half of their EQE and more than 75% of their power conversion efficiency within 24 hours.

We also compared performance of devices stored in air. The dithiol-capped PbSe nanocrystal based devices retained their high EQE and ~ 80% of their PCE over 48 hours, whereas the amine-capped devices lost all performance within the same period of time.

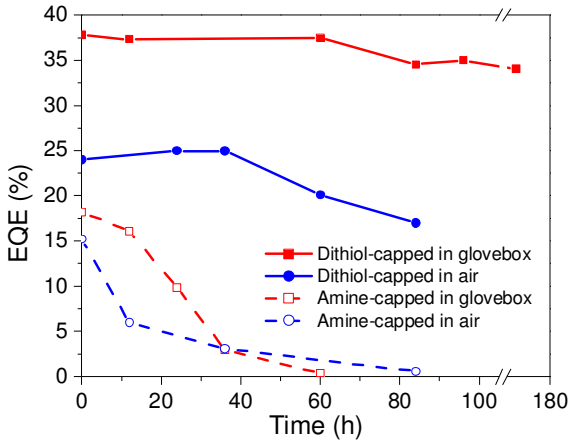


**(a)**

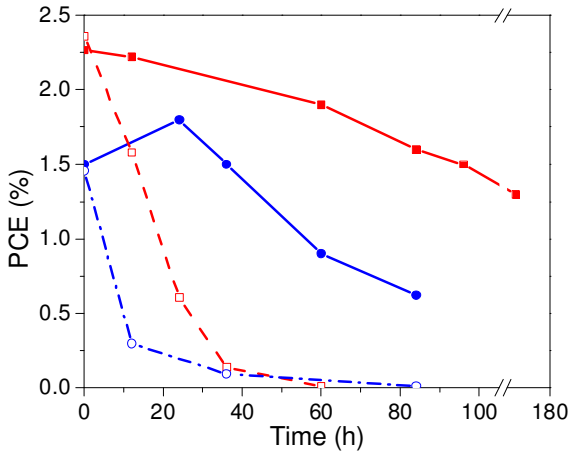


**(b)**

**Figure 5-3 EQE (a) and PCE (b) stability comparison of benzenedithiol treated PbSe nanocrystal devices with previously reported amine-capped devices stored in air and in inert atmosphere [15]. The benzenedithiol treated devices retained their high EQE values for over a week stored in a nitrogen filled glovebox (solid red line), and their PCE maintains 90% of its initial value for more than 2 days. The amine-capped devices (dashed red line) severely deteriorated within the first 24 h. In air, the benzenedithiol treated devices (solid blue lines) registered greater stability than the amine-capped devices (dashed blue lines). Note that all the testing was done in air, and all the devices in this study were exposed to a minimum of 15 hours of oxygen and moisture. Several high efficiency benzenedithiol treated devices retained over 75% of their EQE for more than two weeks. The reported EQE and PCE values were taken under 12 mW cm$^{-2}$ at 975 nm.**

## 5.3 Transport Characteristics

We sought to investigate in greater detail the physical mechanisms responsible for the performance of our best devices. We employed various characterization techniques to determine the transport characteristics of the closed packed nanocrystal films.

### 5.3.1 Charge Extraction by Linearly Increasing Voltage (CELIV)

CELIV has been used to determine the transport properties of inorganic and organic semiconductors [66]. It involves measuring the majority carrier mobility in the photovoltaic devices by applying a pulse of linearly increasing voltage ($U(t)=At$, where A is the pulse slope) and measuring the current transient across the sample with one blocking contact. The current transient signal is indicative of the extraction of the equilibrium charge carriers from the junction; it is a superposition of a displacement current signal with a drift component [66]. The voltage ramp is applied in reverse bias and the majority carriers are extracted from the ohmic contact. In principle, as the voltage increases, the depletion region widens until the semiconductor layer becomes free of charge; at this point, the current signal flattens to its displacement component [66].

The time to reach the extraction current maximum $t_{max}$ was used to estimate the hole mobility. When $\Delta j=j_{max}-j(0)\leq j(0)$, where $j_{max}$ is the maximum value of the current

and j(0) is the displacement current as indicated in Figure 5.4, the hole mobility can be calculated from

$$t_{max} = d\sqrt{\frac{2}{\mu A}}$$

Where d is the film thickness (~230 nm), and $\mu$ is the majority carrier mobility. The mobility was found to be $2.4\text{x}10^{-3}\text{cm}^2\text{V}^{-1}\text{s}^{-1}$ in the PbSe nanocrystal based solar cells reported here. The displacement current step j(0) can be used to evaluate the static relative permittivity $\varepsilon_r$

$$j(0) = \varepsilon_r \varepsilon_0 A/d$$

where $\varepsilon_0$ is permittivity of free space. The static relative permittivity was found to be 15±1. A typical CELIV transient is represented in Figure 5.4.

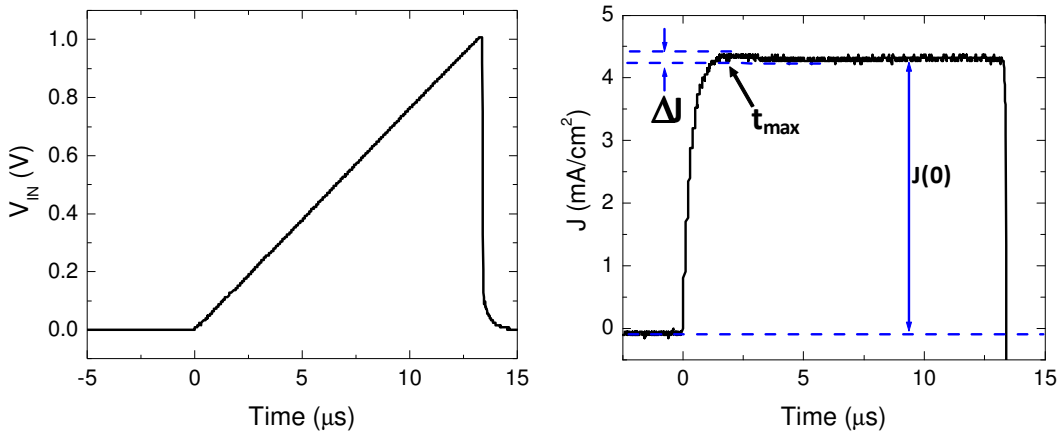


**(a)** **(b)**

**Figure 5-4Typical CELIV transients. In (a), an input pulse of linearly increasing voltage is presented (A=75000 V/s). The output current density transient is depicted in (b). The hole mobility is determined from $t_{max}$.**

CELIV allowed us to determine the mobility of the majority carriers in the photovoltaic devices; we used the time of flight technique to determine the minority carrier mobility.

### 5.3.2 Time-of-Flight (TOF)

In the time of flight technique, the current transient is recorded after subjecting the sample to short optical pulse [67]. The mobility of both charge carriers can be analyzed by controlling the polarity of the applied bias. When a reverse bias is applied, the photo-generated minority carriers drift across the active layer to be extracted.

Time of flight was performed on a sample with a geometry identical to the photovoltaic device, i.e. a layer of nanocrystals sandwiched between the ITO and magnesium contacts, with the exception that the total nanocrystal layer in this case was thicker (> 700 nm) to ensure that the carriers are created in a thin portion of the device. The devices were held under reverse bias by applying a positive potential to the Mg contact and a negative potential to the ITO. The device was fully depleted of equilibrium charge carriers under the applied bias. A 10 ns pulse of 532 nm light was incident on the sample from the transparent ITO side. Under the influence of the applied bias, the photo-generated minority carriers (electrons) drift across the sample to the Mg anode. The transient current generated by the flow of the photocarriers was recorded. In the case of dispersive media such as nanocrystals, the transit time was determined by finding the intersection of two linear regions on a log-log plot of current vs time [67]. Figure 5.5 shows a typical TOF transient plot. The transit time is related to the mobility by $\mu = d^2/V.t_r$ where d is the film thickness and V is the applied bias. The minority electron mobility registered two orders of magnitude increase from almost $1x10^{-5}$ $cm^2V^{-1}s^{-1}$ for an untreated film to $1.4x10^{-3}$ $cm^2 V^{-1}s^{-1}$ for a BDT treated film.

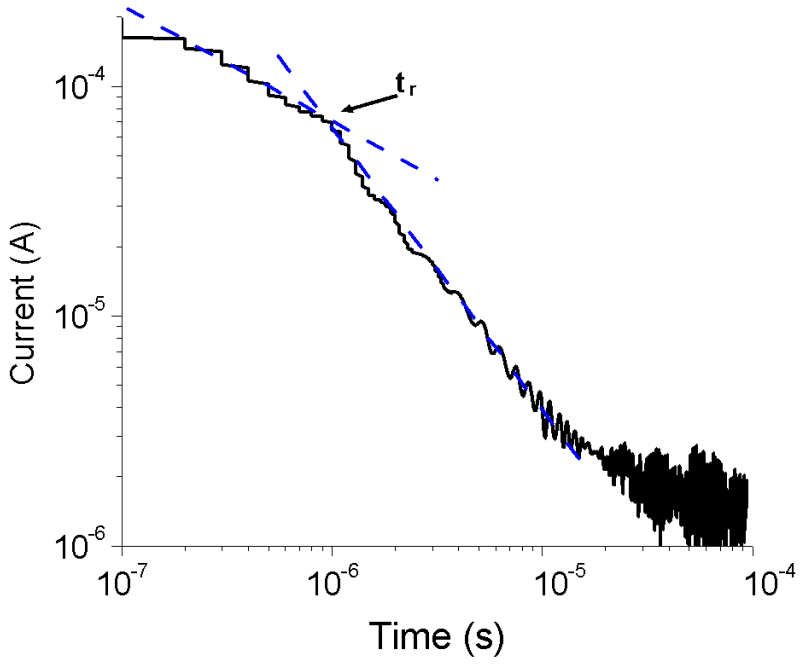


**Figure 5-5 A representative ToF current transient. The intersection of the two linear regions is the transit time $t_r$~1 μs. The sample thickness was 750 nm and the voltage bias was set to 5 V.**

We determined the mobility of both charge carriers in the photovoltaic devices. We now turn to evaluate the carrier recombination lifetime at the relevant intensities.

### 5.3.3 Open-Circuit Voltage Decay (OCVD)

For efficient carrier extraction, the transit time must be shorter than the characteristic time for carrier recombination at the relevant intensities, which was measured using the technique of transient open circuit voltage decay (OCVD) [68]. The OCVD method allows us to determine the charge recombination lifetimes in photovoltaic devices by recording the decay of the open-circuit voltage after abrupt turn-off of the incident light [68]. In open circuit conditions, the photogenerated carriers are not extracted; following illumination turn-off, they will recombine. The open-circuit voltage decay is a direct indication of the recombination rate.

We illuminated the PbSe nanocrystal based device using digitally modulated 975nm diode laser at different intensities (Figure5.6). The voltage generated across the device was recorded as the illumination was abruptly removed (within 3 μs). The recombination lifetime at every intensity was determined by applying a linear fit to the initial $V_{oc}$ decay (d(Voc)/dt). Figure 5.6 shows a typical OCVD transient. We evaluated the recombination from the following relation

$$\tau = C \times \frac{kT}{q} \frac{1}{dV_{oc}/dt}$$

where *k* is the Boltzmann constant, *T* is temperature, *q* is the elementary charge. The coefficient C varies from 1 in low injection regime to 2 in high injection regime and is determined by the carrier concentrations; Without a reliable measure for the carrier concentration, we chose to underestimate our recombination lifetime and set C to 1 for our analysis. At the operating intensity of 12 mW $cm^{-2}$, the lifetime was found to be 13 μs (figure 5.7).

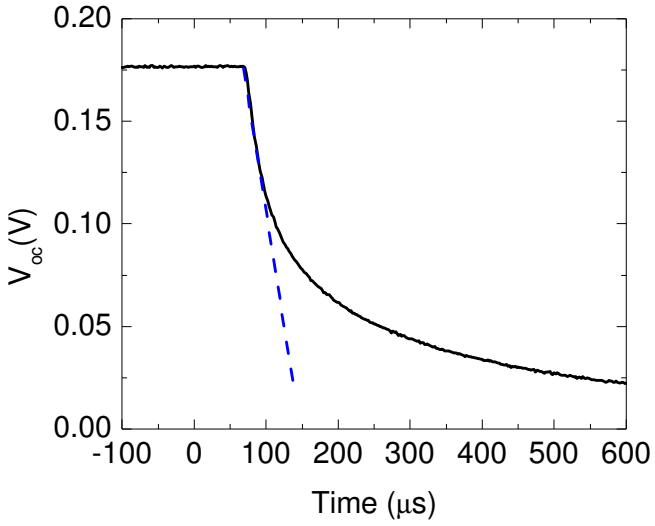


**Figure 5-6 Typical OCVD transient. The recombination lifetime is evaluated from the slope (dashed blue) of the voltage transient decay. From the slope (dashed blue), we estimate the lifetime to be 10 μs at 20 mW $cm^{-2}$.**

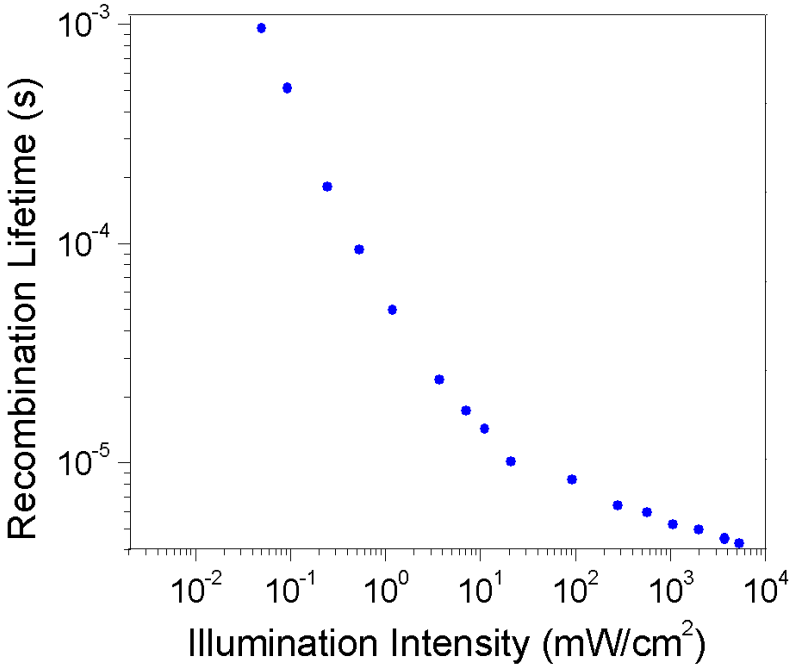


**Figure 5-7 Intensity dependent carrier recombination lifetime**

### 5.3.4 Capacitance at Zero Applied Bias

We measured the capacitance at zero bias under short circuit conditions in order to determine the device depletion width (W). The capacitance value per unit area ($C_i$) was determined to be 2 x $10^{-7}$F $cm^{-2}$.

## 5.4 Conclusion

This chapter detailed the photovoltaic devices performance, their improved stability compared to other colloidal quantum dot based devices, and the transport characteristics of the semiconductor film. The following are the highlights of this chapter:

- We recorded an infrared power conversion efficiency of 3.6% and an external quantum efficiency of 46% at 975 nm under 12 mW $cm^{-2}$ illumination intensity.

- The simulated solar power conversion efficiency was 1.1% under AM1.5 conditions
- Approximately 40 devices recorded infrared power conversion efficiencies of more than 3%
- The external quantum efficiency reached 70% over the visible range and the internal quantum efficiency exceeded 90% at 975 nm.
- The devices retained their high performance for at least two weeks stored in nitrogen without the need of new contacts.
- The hole and electron mobility in the photovoltaic devices are in the same order of magnitude in contrast with recently reported PbS nanocrystal based devices [48]. The electron mobility is about seven times larger.
- The carrier recombination lifetime under low injection regime is 13 us and the capacitance value per unit area under short circuit conditions is $2 \times 10^{-7} F\ cm^{-2}$.

The next chapter will be dedicated to explain the physical mechanism of the devices reported herein and the origin of high external quantum efficiencies. The transport characteristics evaluated in this chapter will be used to that end.

# 6 Model of Physical Mechanisms and Origins of High Efficiency

In this chapter, we investigate in greater detail the physical mechanisms responsible for the performance of our best devices, and the process steps that were most critical to the performance improvements reported herein.

In a metal-semiconductor-metal solar cell, a Shottky barrier is ideally formed at one of the interfaces while the other contact serves as an ohmic junction. At the Shottky barrier, a depletion region is formed and a built-in field is established. In principle, the electron-hole pairs are photogenerated within the entire active layer; they diffuse towards the depletion region where the field sweeps away the minority carrier towards the rectifying junction while the majority carrier diffuses throughout the active layer to be extracted by the ohmic contact. Recombination losses will be present.

In our analysis, we begin with an exploration of which metal-semiconductor junctions is responsible for providing rectification and charge separation. We then estimate from capacitance-voltage measurements the spatial extent of the resultant depletion region. From this we are able to propose a spatial band diagram.

We then quantify the absorbance of photons in each of the key regions – the depletion and quasi-neutral portions – of the colloidal quantum dot active region. Combining this with knowledge of the depth of the depletion region, the thickness of the device, and the measured EQE, we are able to estimate the minority carrier diffusion length that is required to explain our high overall efficiency.

We then proceed to investigate whether the electronic properties of our materials are indeed capable of supporting such a long minority carrier diffusion length. We

estimate an electron diffusion length in the range 200-300 nm, and find this to be sufficient to account for our high observed efficiencies.

## 6.1 Rectifying Junction and Location of Depletion Region

We turn first to our investigations of the location of the rectifying metal-semiconductor junction, and thus the depletion region, in our devices. We studied this by varying the choice of metal both as bottom and top contact. First, while maintaining ITO as the bottom contact, we deposited Al (~4.2 eV) , Ag (~4.3 eV), or Mg (~3.6 eV) atop the NC films. In all cases we obtained similar I-V characteristics, though the open circuit voltages ($V_{oc\_Mg}$>$V_{oc\_Al}$>$V_{oc\_Ag}$) were smaller when Ag and Al were used. On the other hand, when we employed Au as top contact, the device exhibits a linear I-V (Figure 6.1).

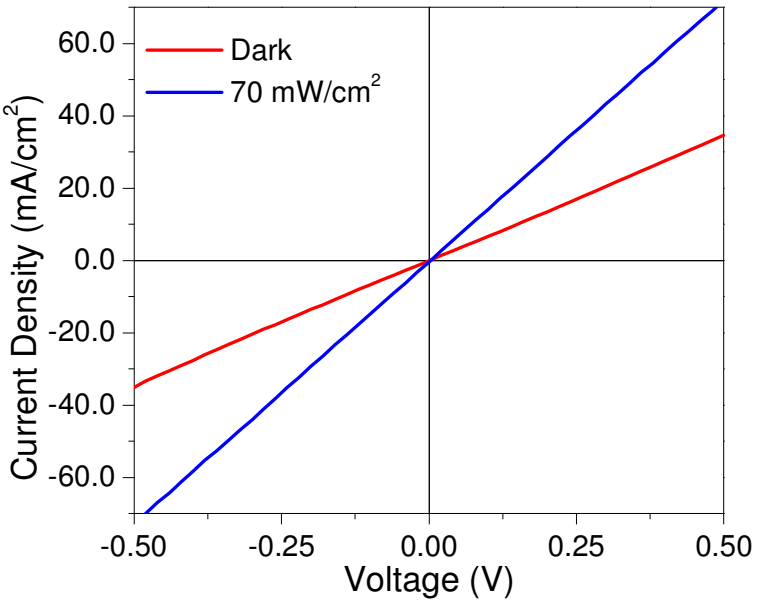


**(a)**

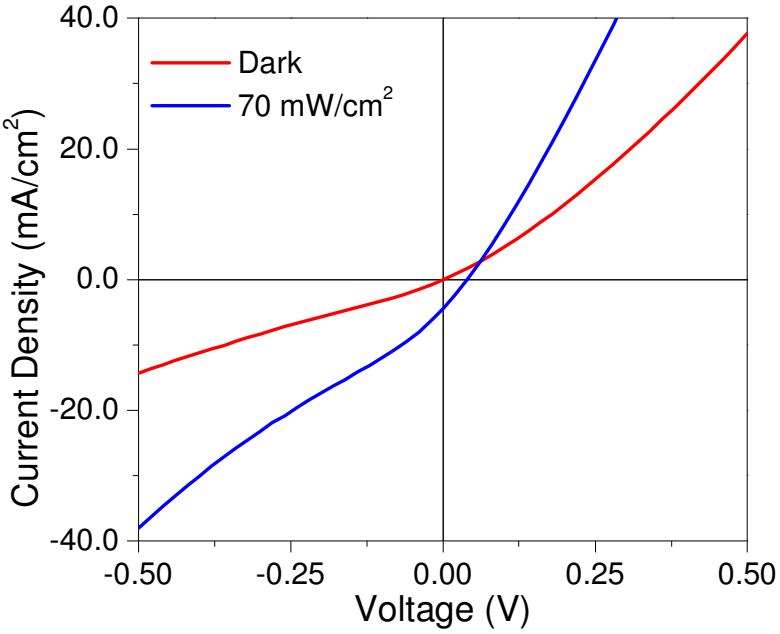


**(b)**

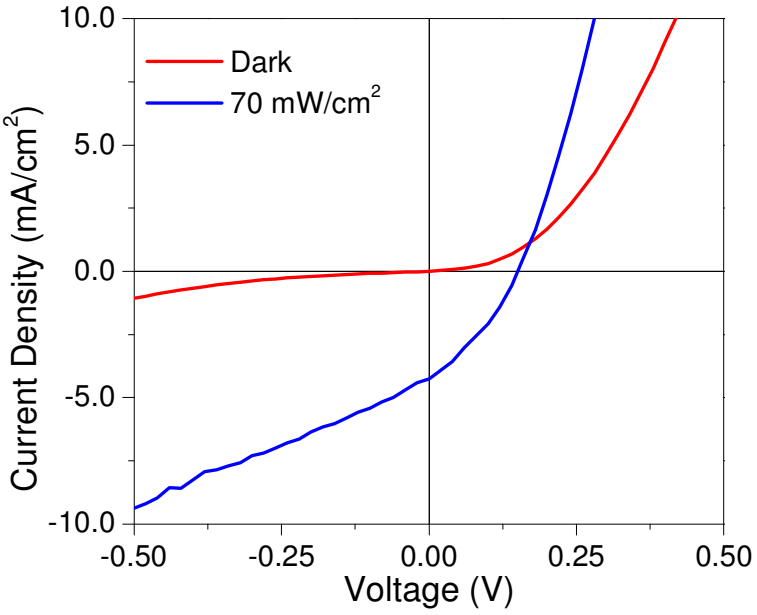


**(c)**

**Figure 6-1 Current-Voltage Characteristics of BDT treated PbSe CQD devices with bottom ITO contact and with (a) Au, (b) Ag, and (c) Al top contacts.**

From this we concluded that the Mg-NC junction is responsible for rectification in our devices. We also varied the bottom contact, replacing ITO (~4.8 eV) with Pt (~6.3

eV) or Au (~5 eV). All devices continued to provide good rectification when a Mg top contact was employed; and the current-voltage characteristics did not appreciably change. From this we concluded that the bottom contact (transparent ITO in our best devices) serves mainly for ohmic hole collection in our solar cells. Based on these conclusions we propose the spatial band diagram of Figure 6.2.

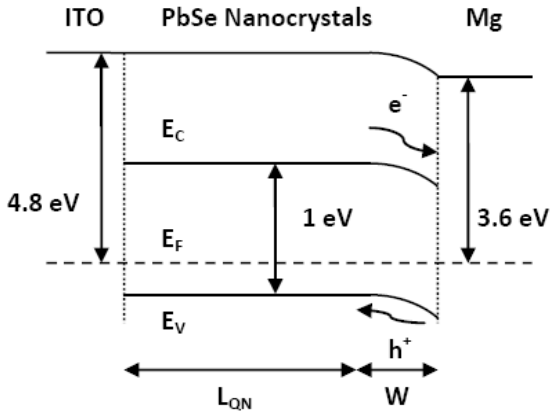


**Figure 6-2 Spatial band diagram showing the device model. A Schottky barrier is formed at the Mg/p-type semiconducting NCs interface. The majority of the photogenerated carriers diffuse through the quasi-neutral region ($L_{QN}$~145 nm) and are separated in the depletion region (W~65 nm). A fraction of the carriers is lost to recombination.**

We sought then to determine the depth of the depletion region associated with the Mg-NC junction. From the capacitance value per unit area (Ci) at zero bias and the static relative permittivity ($\varepsilon_r$) determined in the last chapter, we were able to estimate the depletion width, $\varepsilon_r \varepsilon_0$ /Ci, to be 65±5 nm where $\varepsilon_0$ is the permittivity of free space.

We fabricated thin film field-effect transistors (FET) on highly conductive silicon wafers with 100 nm of thermally grown oxide as the gate dielectric. The source and drain electrodes were separated by a 10 μm gap. In order to spin-coat 50 nm thick films, we diluted the octylamine-capped PbSe nanocrystals to a concentration of 10 mg $mL^{-1}$and the benzenedithiol solution to 1 mM. For constant drain source voltage, we applied a

range of gate voltages and recorded the current modulation through the nanocrystal film. The detailed analysis of these experiments was reported by Harnik Shukla [70].

Figure 6.3 shows the FET transfer characteristics of nanocrystal films directly deposited from solution and after exposure to benzenedithiol treatment. In both cases, the drain current ($I_d$) increases in magnitude as the applied gate voltage ($V_{gs}$) becomes more negative. This suggests the formation of a p-channel in the FET devices indicative of the p-type behavior of the PbSe nanocrystals [69]. The conductance (G) of the NC films, equated to the slope of the $I_d$-$V_d$ graph at zero gate bias (inset of Figure 6.3), increased after the film treatment. The majority carrier mobility also experienced an improvement after BDT treatment.

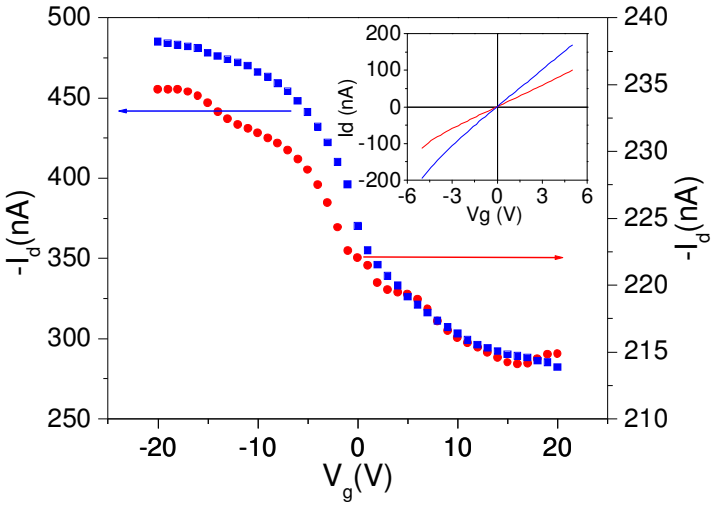


**Figure 6-3 Transfer characteristics of PbSe nanocrystal thin film field-effect transistors. The PbSe nanocrystal films exhibit p-type behaviour before (red) and after benzenedithiol treatment (blue). $I_d$-$V_d$ characteristics for both films are shown in the inset. The conductivity, which can be induced from the slope of the $I_d$-$V_d$ curves, increased after treatment.**

## 6.2 Photon Absorption

Having elucidated a simple spatial band diagram, we sought to determine where electron-hole pairs were generated, and in which quantities, within the two regions of interest – the depletion region, with its charge-separating field, and the quasi-neutral region, in which minority carrier diffusion would serve as the dominant transport mechanism.

We first looked at whether absorption within the depletion region could, on its own, account for our high observed EQEs. For the total absorption measurements, we measured the reflectivity of the substrate and corrected for the ITO (~5%) and Mg contact absorption (~4%) (Refer to Appendix C). In the case we are considering in our following analysis, the percentage of light absorbed in a 210 nm thick photovoltaic device at 975 nm was 43% and the corresponding mean external quantum efficiency was 32%. We are assuming that the light absorbed through the ITO contact was reflected back at the mirror-like upper metallic contact. Thus, assuming a uniform light absorption profile, the fraction of light absorbed incident from the ITO side in double pass is:

$$A_{total} = 1 - e^{-2\alpha d}$$

where d is the thickness of the CQD film, and α is the absorbance.

The percentage of photons absorbed through the depletion region of 65 nm width near the Mg contact in double-pass is estimated to be 13%. Accordingly, the electron-hole pairs generated in the depletion region, believed to be efficiently extracted (> 90%), only contributed to less than half of the photocurrent. The quasi-neutral region absorbed the remaining 30% of the incident light. In order to account for the 32% EQE at 975 nm, 20% of the photogenerated carriers created in the quasi-neutral portion of the device must

have diffused to the depletion region to be separated therein. The rest was lost to carrier recombination. Minority carrier diffusion must be playing a large role in our devices. The model presented herein is depicted in figure 6.4.

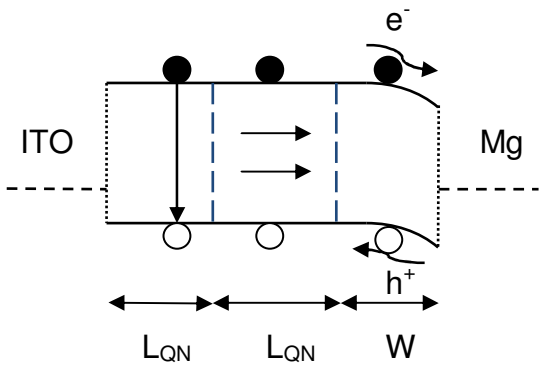


**Figure 6-4 Schematic diagram of our analytical model. The electron-hole pairs generated within the depletion region (W) are efficiently separated. The electrons generated within $L_{QN2}$ diffuse to the depletion region where they are separated by the built-in field while the electrons generated within $L_{QN1}$ of the ITO contact are mostly lost to recombination.**

From our knowledge of the absorption per unit length of 975 nm light, we summarize in Table 2 the fraction of incident power absorbed in each region. We conclude from this that less than half of the observed short-circuit current is attributable to electron-hole pair generation from absorption within the depletion region.

**Table 2 Summarizing the contribution of the depletion and quasi-neutral regions to the EQE under 12 mW cm$^{-2}$ intensity at 975 nm.**

| Region | Relevant Thickness (nm) | Absorption (%) | IQE (%) | Percentage Contributed to Overall EQE |
|---|---|---|---|---|
| Depletion | 65 | 13 | > 90% | > 12 |
| Quasi-neutral | 145 | 30 | 65 | 20 |
| | | | Total Measured EQE: | 32% |

Assuming that the electron-hole pairs which are nearest to the depletion region have a larger chance to diffuse and separate, the photons absorbed in $L_{QN2}$ of thickness ~95 nm account for the rest of the EQE. In order to estimate the required diffusion length for the least mobile carrier (electrons in our case), we assume that only the photogenerated carriers in the quasi-neutral region that have a transit time of 0.1 $\tau$ ($L_{QN2}$ ~95 nm), where $\tau$ is the recombination lifetime, must have diffused to the depletion region to be efficiently separated therein and extracted therefrom. We estimate that the model is plausible within experimental uncertainty if the minority carrier diffusion length is in the 200 – 300 nm range.

## 6.3 Drift and Diffusion Lengths

To evaluate the feasibility of the electron and hole drift over the depletion region depth (~65 nm) and the electron minority carrier diffusion over the quasi-neutral region depth (~145 nm), we next turned to the estimation of the drift and diffusion lengths.

Carriers in the depletion region are separated via the action of the built-in field resultant from the metal-semiconductor, or Schottky, junction. The drift length is given by $\frac{\mu\tau V_{bi}}{W}$ where $\mu$ is the carrier mobility, $V_{bi}$ is the built in potential, and W is the depletion width. Under short circuit conditions at 12 mW $cm^{-2}$, and assuming a built in voltage of 0.3 V [47,48], we estimated drift lengths of 8.5 μm for electrons and 14.5 μm for holes. In sum, we expect no difficulty in removing each carrier type from the 65 nm thick depletion region. In the quasi-neutral region, charge transport occurs mainly through diffusion and the carrier diffusion length may be obtained from $\sqrt{\mu\tau\frac{kT}{q}}$. The calculated electron minority diffusion length is in excess of 220 nm, which allows a substantial fraction of the minority carriers to diffuse out of the neutral region, and allows us to account for the high observed EQE as we proposed earlier in this chapter. Table 4 summarizes the calculated charge transport characteristics.

**Table 3 Summary of the charge transport parameters for the benzenedithiol treated PbSe NCs based photovoltaic devices at the operating intensity of 12 mW $cm^{-2}$ at 975 nm and under low injection regime.**

| Carriers | Mobility($cm^2$/Vs) | Recombination Lifetime ($\mu s$) | Drift Length ($\mu m$) | Diffusion Length (nm) |
|---|---|---|---|---|
| Electrons | $1.4 \times 10^{-3}$ | >13 | 8.5 | 220 |
| Holes | $2.4 \times 10^{-3}$ | >13 | 14.5 | 285 |

Carrier extraction in these photovoltaic devices, due to the narrow depletion region, is critically dependent on diffusion enabled by high minority carrier mobility and long lifetime. This contrasts with recent findings in drift-dominated PbS Schottky-barrier devices [48].

We further corroborated our proposed physical picture by investigating the dependence of EQE and recombination on illumination intensity, as seen in Figure 6.5. The EQE began to diminish at intensities greater than 10 mW $cm^{-2}$. From OCVD measurements, the recombination lifetime drops below about 10 μs at such intensities. In view of the electron mobility, the electron diffusion length begins to contract well below the quasi-neutral region thickness under such conditions, accounting for the onset of EQE roll-off.

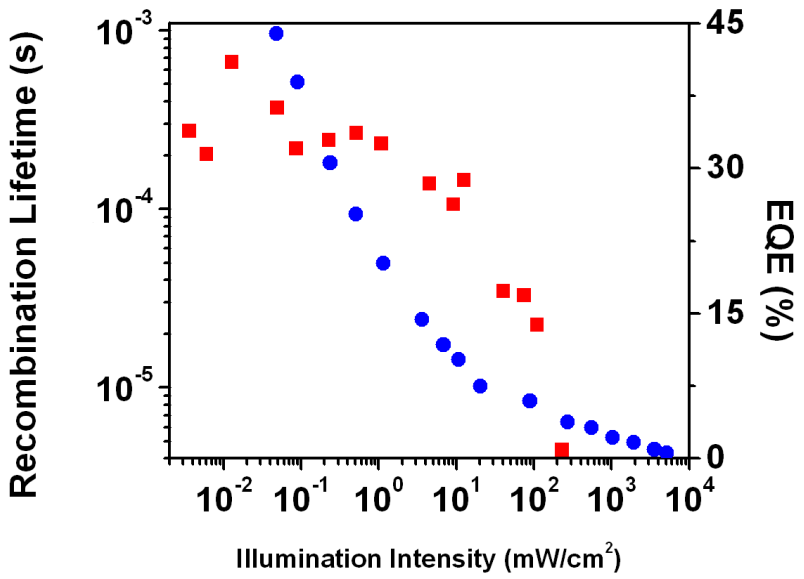


**Figure 6-5 Carrier recombination lifetime (blue, left axis) and external quantum efficiency (red, right axis) versus illumination intensity at 975 nm. The decrease in the EQE (>10 mW cm$^{-2}$) corresponds to the limit where the minority carrier transit time exceeds the recombination lifetime.**

## 6.4 The Role of Benzenedithiol

With this performance and physical picture explained, we now discuss the role of our chosen bidentate linker. The first expected impact of linking nanoparticles in the solid state is to bring the particles closer together (figure 6.6). Figure 4.2 (a) shows that benzendithiol molecules are most likely crosslinking the PbSe nanoparticles. Specifically, both electron and hole mobilities have increased by more than an order of magnitude as a result of crosslinking. Even with the mobility-increasing treatments, the films retained their quantum size effect, as seen in absorption spectra and external quantum efficiency spectra.

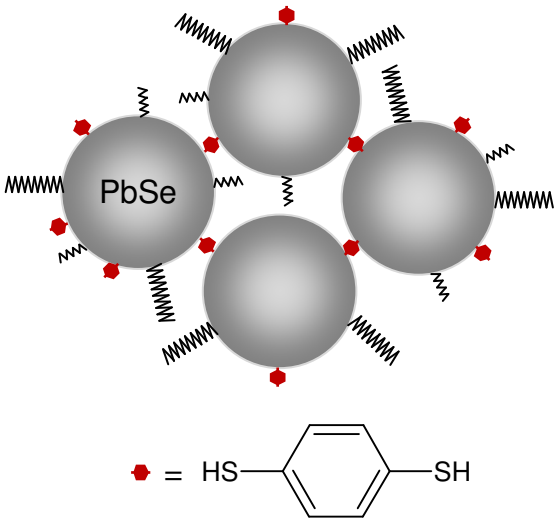


**Figure 6-6 Crosslinked PbSe nanocrystals**

We noted above that diffusion plays a much larger role in our devices than in the best reported PbS nanocrystals solar cells. The electron mobility of our devices is seven times greater than in the PbS colloidal quantum dot report [48], a fact which accounts for a doubling of the electron diffusion length in our materials system. Benzenedithiol is in fact a molecular conductor in view of its delocalization of electron molecular orbitals [64]. In addition, conjugated dithiol molecules used to bridge quantum dot systems have previously been reported not only to link nanocrystals, but also to provide a pathway for electron transfer [65].

The devices reported herein exhibited a photovoltaic response only after being subjected to the benzenedithiol crosslinking process. We propose that the as-exchanged nanocrystals were dominated by a large density of unpassivated surface states. As with previously-reported chemical processes on PbSe and CdSe nanocrystals [51-54, 61-63], benzenedithiol offers passivation of dangling bonds. Additionally, as seen in our stability study, benzenedithiol appears to offer a longer-lived nanocrystals/metal interface than amine ligands. The latter are believed to react with the top metal contact.

Another feature of the device processing architecture employed herein is the use of two superimposed layers of colloidal quantum dot solids. Our purpose was to increase absorbing thickness and minimize pinholes. Preceding the solid-state treatment with a solution-phase exchange to a somewhat shorter ligand helped to reduce volume contraction upon crosslinking of the film. This contributed to the realization of densely-packed, high-mobility films in situ on a substrate. A further improvement would be using a multi-layered treated device where the mobility of the minority carrier is orders of magnitude higher than ours.

## 6.5 Conclusion

This chapter primarily aimed at presenting a model of the physical mechanisms of the photovoltaic devices and the origins of high performance. We propose a spatial band diagram and plausible model explaining the observed high external quantum efficiencies. The main conclusions of this chapter are summarized as follows:

- The Shottky barrier is formed at the semiconductor/Mg contact while the ITO serves as a hole collecting ohmic contact; The depletion width is estimated to be 65±5 nm.
- The nanocrystals behave as p-type semiconductors before and after treatment.
- The photogenerated carriers in the depletion region only contribute to one third of the external quantum efficiency; Diffusion of the carriers from the quasi-neutral region is suspected to play a major role. The calculated minority carrier diffusion length of 210 nm is sufficient to make our model plausible. We also conclude that further improvement in performance could be achieved by increases in electron

mobility leading to even more efficient diffusion from the quasi-neutral region to the edge of the depletion region.

- At 10 mW $cm^{-2}$, the external quantum efficiency decrease was attributed to the fact that the photocarrier transit time starts exceeding the recombination lifetime.
- The benzenedithiol molecule is at the origin of high efficiency in our devices; the increase in carrier mobility after treatment, the exceptionally high final electron mobility, and the stability of the photovoltaic devices directly result from the use of BDT.

In sum, the present work demonstrates a stable, high-efficiency infrared solution-processed photovoltaic device. Remarkably, the work shows that minority carrier diffusion can occur efficiently over hundreds of nanometers in such films. Strongly-passivating, short, electron-transport-assisting bidentate linkers appear to play a key role in achieving these properties.

# 7 Summary

We summarize the major findings of our work in this chapter. We will also discuss the significance of these contributions to the field of large-area photovoltaics, and close with a presentation of avenues for future research.

## 7.1 Thesis Objectives

We stated in chapter 1 the main objective of this thesis as **the demonstration of the first stable, efficient infrared solution-processed photovoltaics.** We achieved this goal, specifically through the use of benzenedithiol crosslinkers that stabilized a PbSe colloidal quantum dot active region in a Schottky architecture.

The motivation for infrared sensitive solution-processed photovoltaic conversion was presented in chapter 1. Chapter 2 aimed to position this research within the context of other work in related areas. Theoretical concepts and device architectures of solution-processed materials were examined along with solar cell essentials. We also presented the strategy we pursued to achieve high efficient stable devices: Amine nanocrystal-capping ligands were found to be labile as to imperil the stable passivation of thin solid films over days and weeks; we therefore selected strongly-binding electron conducting end functional group to passivate our nanoparticle surfaces robustly in the solid state and improve carrier transport.

Chapter 3 described the chemical processing of the PbSe nanocrystals in solution form; we were successful in establishing for the first time in the Sargent group a reliable PbSe nanocrystal synthesis process followed by a solution-based ligand exchange aimed

at reducing the inter-nanoparticle distance for improved electrical properties. We described the device fabrication process in chapter 4. The deposition process of the nanocrystal films and the solid state processing that proved to be necessary to obtain efficient photovoltaic devices were both presented. The crosslinking process was optimized for maximum efficiency by careful variation of the treatment duration. Chapter 5 presented a detailed account of the devices photovoltaic performance, their stability, and carrier transport characterization. The devices achieved 3.6% infrared power conversion efficiency and retained their high efficiency for two weeks stored in nitrogen. Carrier transport parameters were evaluated in chapter 5 and later used in Chapter 6 to build a physical mechanism model. The electron and hole mobilities were in the same order of magnitude in contrast to recent findings for PbS nanocrystal based devices. The carrier recombination lifetime and the zero bias capacitance were also determined. In chapter 6, we investigated in greater detail the physical mechanisms responsible for the performance of our best devices. We determined that the Mg/semiconductor junction was responsible for providing rectification and charge separation. The capacitance measurement was used to evaluate the ~65 nm depletion region and a spatial diagram was proposed. We evaluated the photon absorption in each region of the device and estimated the required diffusion lengths to explain our device efficiencies. We later proved that the electronic properties of our devices are indeed capable of supporting long diffusion lengths and thus account for the high efficiencies observed. Diffusion of carriers rather than drift was the dominant transport mechanism in our devices. We concluded the chapter by describing the role of the benzenedithiol molecule. The latter provided the

necessary passivation for improved stability, crosslinked the nanocrystals, and facilitated electron conduction for improved carrier transport.

## 7.2 Contribution to the field

This work reports noteworthy advances in the infrared sensitive solution processed photovoltaic research area. The first efficient PbSe nanocrystal based photovoltaic devices are reported herein: they provide a more-than-ten-fold improvement in infrared power conversion efficiency compared to the previous record [17,18]. They also represent the first infrared solution-processed photovoltaic devices to report stability over greater than two weeks.

The devices reported herein combine the simple Shottky junction architecture with the ease of fabrication of solution processed materials. The crosslinking treatment employed allows nanocrystal layer stacking which could potentially be very useful in multijunction solar cell designs. As stand-alone solar cells, our devices performed remarkably well in the infrared and could be optimized in that regard.

## 7.3 Closing Remarks

This thesis represents substantial improvement in stable efficient infrared solution processed photovoltaics. Further progress can be achieved by optimizing chemical and fabrication processes. The following are potential future possible directions to improve efficiency:

- It is clear that further improvement in carrier mobility and thus longer diffusion lengths is necessary: this would enable additional light absorption in thicker devices and thus more photons to be converted to electrons. This could be

achieved by optimizing synthesis as well as solution-phase and solid-state treatments.

- The carrier extraction efficiency could be enhanced by optimizing the carrier lifetimes. An understanding of the surfaces states dominating our materials and controlling them by means of effective passivation is urgently needed in this regard.
- Controlling the doping levels in the material system would allow the fabrication of p-n junctions. These have previously been shown to be more efficient than Shottky barriers in related inorganic bulk semiconductor photovoltaics research.
- Ultimately, high efficiency will require an all-solution-processed nanocrystal tandem cell that includes an efficient infrared cell as the lowest band gap junction. Future research must include the integration of the optimal 1300 nm bandgap cell presented herein with its larger-energy-photon-harvesting 850 nm top layer.

These promising directions suggest that our current research is just the beginning and dramatic improvements will occur in the near future. Infrared colloidal nanocrystal photovoltaics are in their infancy: many opportunities remain to be explored for them to realize their full impact.

# Appendix A: Chemicals

Lead (II) oxide powder (PbO, 99%), Oleic acid (OA, technical grade 90%), 1-Octadecene (ODE, technical grade 90%), anhydrous toluene, octane, methanol, isopropanol, acetonitrile, and ethyl acetate were purchased from Sigma-Aldrich. Bis(trimethylsilyl)selenide (TMSe) , > 97% purity was purchased from Gelest, Inc. 1,4 benzenedithiol (97%) was purchased from Alpha Aesar.

# Appendix B: Device fabrication, testing, and characterization.

The octylamine-exchanged PbSe NCs were spin-coated at a speed of 500 rpm on ITO-coated glass substrate (CG-90IN) inside the glovebox. The devices had a typical thickness of 210 to 250 nm as measured with a surface profiler (Veeco Dektak3). The benzenedithiol treatment was done in a fumehood in air. We deposited 100 nm Mg/190 nm Ag by thermal evaporation through a shadow mask, leading to a contact area of 3.1 $mm^2$. We stored the devices in a nitrogen filled glovebox for 24 h before initial testing. All device characterizations were carried out in dark shielded enclosures in air.

All current-voltage measurements including FET characterizations were taken with an Agilent 4155C semiconductor parameter analyzer. For the IR characterizations, the devices were illuminated through the ITO-coated glass using a continuous-wave diode laser operating at 975 nm. An Oriel solar simulator operating at 100 mW $cm^{-2}$ was used to simulate the solar spectrum under AM1.5 conditions. The illumination intensity was measured with a Melles-Griot broadband power meter.

For the TOF measurements, thick samples (>600nm) were excited using a Yttrium-Aluminum-Garnet (YAG) laser operating at 532 nm with 10 ns pulses at a 10 Hz repetition rate. The light was incident on the sample from the transparent ITO side. The devices were biased using a Keithley 2400 Source Meter, and a digital oscilloscope was used to measure the current transient output across a 50 Ω load. The CELIV measurements were carried out using an Agilent 33120A function generator which provided the linearly increasing voltage signals and the current output was measured across a 50 Ω load with a Tektronix TDS 220 digital oscilloscope.

The OCVD transients were recorded using a digital oscilloscope with a 1 MΩ input impedance. The illumination source (975 nm diode laser) was modulated using a Stanford Research Systems DG535 digital pulse generator. An Agilent 4284A LCR meter was used to measure the capacitance at zero bias in order to determine the device depletion width.

For the external quantum efficiency spectrum measurements, the incident light was chopped at 100 Hz and the short-circuit current was measured with a Stanford Research SR830 lock-in amplifier. Illumination was provided by a white light source dispersed by a Jobin-Yvon Triax 320 monochromator. The light intensity was kept constant for all wavelengths. The measured spectrum was then scaled to match the value of the monochromatic EQE obtained at 975 nm.

We obtained the total film absorbance by measuring the reflectivity of the substrate and correcting for the ITO and Mg contact absorption in an integrating sphere. A Cary 500 UV-Vis-IR Scan photospectrometer in the reflective mode was used to measure the reflectivity spectra. TEM images were taken using a Hitachi HD-2000.

Appendix C: Contacts Reflectivity Spectra

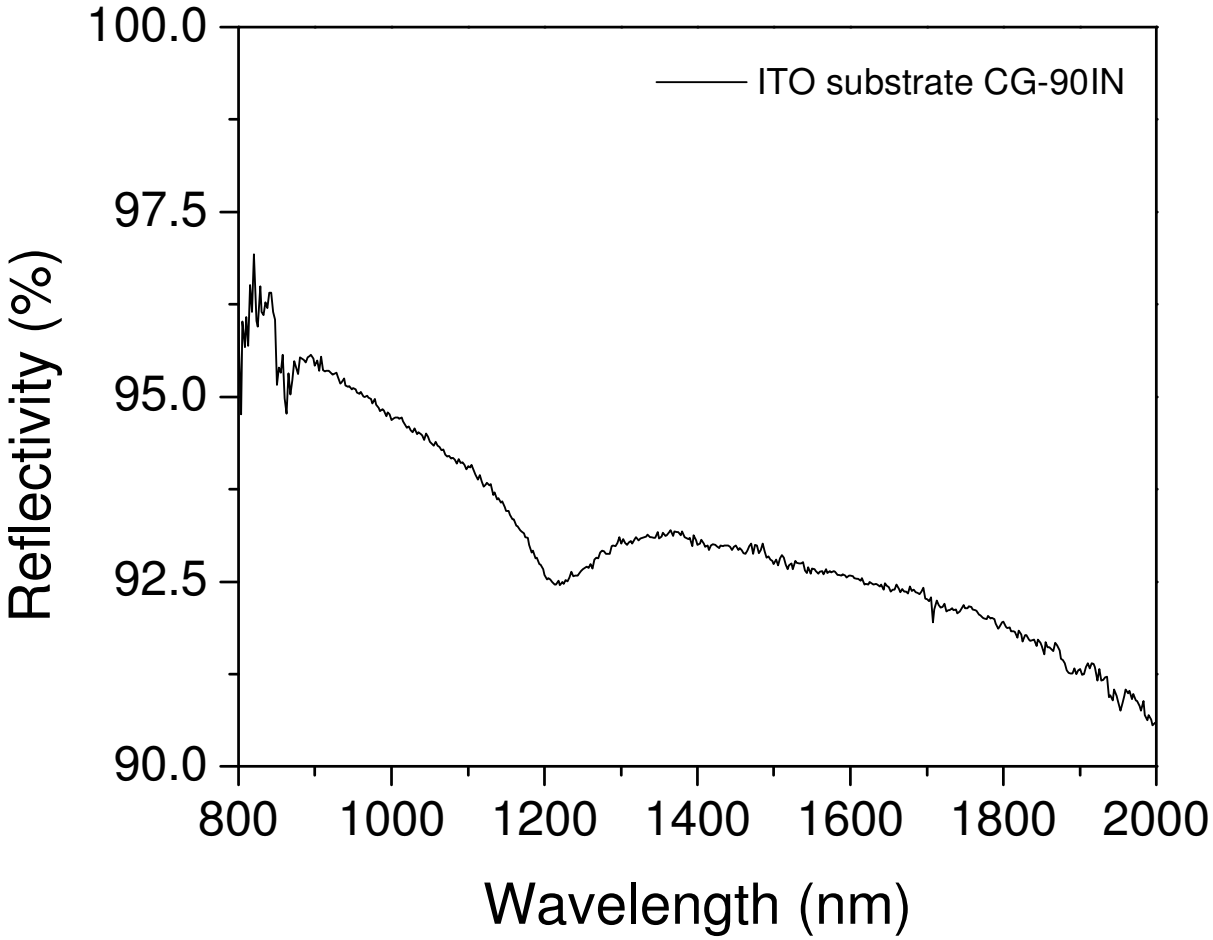

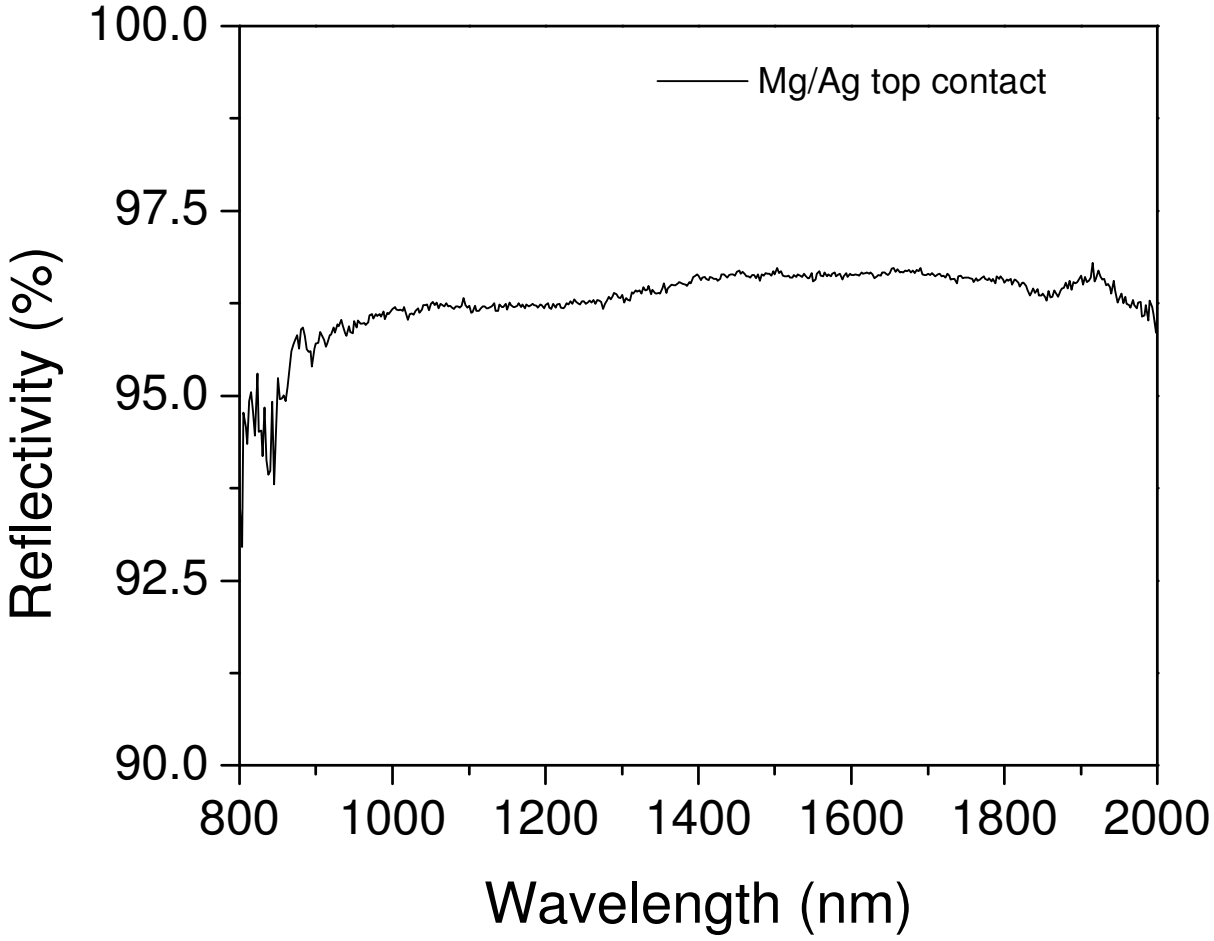
100.0
97.5
95.0
92.5
90.0
Reflectivity (%)
800
1000
1200
1400
1600
1800
2000
Wavelength (nm)
Mg/Ag top contact

# References


1. The UN World Commission on Environment and Development. Our Common Future. The Brundlant report, **1987**.
2. Wurfel, P. Physics of Solar Cells: From Principles to New Concepts. **2005**.
3. Goldemberg, J. Energy Choices Towards a Sustainable Future. *Env.*, **2007**, *49*.
4. Hegedus, S. Status, Trends, Challenges and the Bright Future of Solar Electricity from Photovoltaics. *Handbook of Photovoltaic Science and Engineering* **2003**, chap. 1.
5. Smestad, G. P. Optoelectronics of Solar Cells. *SPIE* **2002**.
6. Nelson, J. The Physics of Solar Cells. *Imperial College Press* **2003**.
7. Kim, K.; Liu J.; Namboothiry, M. A. G.; Carroll, D. L. Roles of Donor and Acceptor Nanodomains in 6% Efficient Thermally Annealed Polymer Photovoltaics. *Appl. Phys. Lett.* **2007** *90*, 163511.
8. Gur, I.; Fromer, N. A.; Geier, M. L.; Alivisatos, A. P. Air-stable All-inorganic Nanocrystal Solar Cells Processed from Solution. *Science* **2005** *310*, 462-465.
9. Gur, I.; Fromer, N. A.; Chen, C.; Kanaras, A. G.; Alivisatos, A. P. Hybrid Solar Cells with Prescribed Nanoscale Morphologies Based on Hyperbranched Semiconductor Nanocrystals. *Nano Lett.* **2007** *7*, 409-414.
10. Sargent, E. H. Infrared Quantum Dots. *Adv. Mater.* **2005** *17*, 515-522.

11. McDonald, S. A.; Konstantatos, G.; Zhang, S.; Cyr, P. W.; Klem, E. J. D.; Levina, L.; Sargent, E. H. Solution-processed PbS Quantum Dot Infrared Photodetectors and Photovoltaics. *Nat. Mater.* **2005** *4*, 1-5.

12. Konstantatos, G.; Howard, I.; Fischer, A.; Hoogland, S.; Clifford, J.; Klem, E.; Levina, L.; Sargent, E. H. Ultrasensitive Solution-cast Quantum Dot Photodetectors. *Nature* **2006** *442*, 180-183.

13. Marti, A.; Araujo, G. L. Limiting Efficiencies for Photovoltaic Energy Conversion in Multigap Systems. *Sol. Energy Mater. Sol. Cells* **1996** *43*, 203-222.

14. Klem, E. J. D.; MacNeil, D. D.; Cyr, P. W.; Levina, L.; Sargent, E. H. Efficient Solution-processed Infrared Photovoltaic Cells: Planarized All-inorganic Bulk Heterojunction Devices via Inter-quantum-dot Bridging during Growth from Solution. *Appl. Phys. Lett.* **2007** *90*, 183113.

15. Johnston, K. W.; Pattantyus-Abraham, A. G.; Clifford, J. P.; Myrskog, S. H.; MacNeil, D. D.; Levina, L.; Sargent, E. H. Schottky-quantum Dot Photovoltaics for Efficient Infrared Power Conversion. *Appl. Phys. Lett.* **2008** *92*, 151115.

16. Koleilat, G. I.; Levina, L.; Shukla, H.; Myrskog, S. H.; Hinds, S.; Pattantyus-Abraham, A. G.; Sargent, E. H. Efficient, Stable Infrared Photovoltaics Based on Solution-Cast Colloidal Quantum Dots. ACS Nano **2008** *2*, 833–840.

17. Cui, D.; Xu, J.; Zhu, T.; Paradee, G.; Ashok, S.; Gerhold, M. Harvest of Near Infrared Light in PbSe Nanocrystal-polymer Hybrid Photovoltaic Cells. *Appl. Phys. Lett.* **2006** *88*, 183111.

18. Jiang, X.; Schaller, R. D.; Lee, S. B.; Pietryga, J. M.; Klimov, V. I.; Zakhidov, A. A. PbSe Nanocrystal/Conducting Polymer Solar Cells with an Infrared Response to 2 Microns. *J. Mater. Res.* **2007** *22*, 2204-2210.

19. Burroughes, J.; Jones, C.; Friend, R. New Semiconductor Device Physics in Polymer Diodes and Transistors. *Nature* **1988** *335*, 137.

20. Garnier, F.; Hajlaoui, R.; Yassar, A.; Srivastava, P. All-Polymer Field-Effect Transistor Realized on Printing Techniques. Science **1994** *265*, 1682.

21. Yu, G.; Gao, J.; Hummelen, J. ; Wudl, F. ; Heeger, A. Polymer Photovoltaic Cells: Enhanced Efficiencies via a Network of Internal Donor-Acceptor Heterojunctions. *Science* **1995** *270*, 1789.

22. Braun, D.; Heeger, A. Visible Light Emission from Semiconducting Polymer Diodes. *Appl. Phys. Lett.* **1991** *58*, 1982.

23. Greenham, N.; Moratti, S.; Bradley, D.; Friend, R.; Holmes, A. Efficient Light-Emitting Diodes Based on Polymers with High Electron Affinities. *Nature* **1993** *365*, 628.

24. Mozer, A. J.; Sariciftci, N. S.; Chap 10: Conjugated Polymer–Based Photovoltaic Devices. *Conjugated Polymers: Processing and Applications* **2007**.

25. Hoppe, H.; Sariciftci, N. S. Organic solar cells: An overview. *J. Mater. Res.* **2004** *19.*

26. Tang, C. W. Two-Layer Organic Photovoltaic Cell. *Appl. Phys. Lett.* **1986** *48*, 183.

27. Peumans, P.; Uchida, S.; Forrest, S. R. Efficient Bulk Heterojunction Photovoltaic Cells Using Small-molecular-weight Organic Thin Films. *Nature* **2004** *428*, 911 – 918.

28. Kim, J. Y.; Lee, K.; Coates, N. E.; Moses, D.; Nguyen, T.; Dante, M.; Heeger, A. J. Efficient Tandem Polymer Solar Cells Fabricated by All-solution Processing. *Science* **2007** *317*, 222-225.

29. Lungenschmied, C. ; Dennler, G.; Neugebauer, H.; Sariciftci, N. S.; Glatthaar M.; Meyer T.; Meyer A. Flexible, long-lived, large-area, organic solar cells. *Solar Energy Materials & Solar Cells* **2007** *91* , 379–384.

30. Wienk, M. M.; Turbiez, M. G. R.; Struijk, M. P.; Fonrodona, M.; Janssen, R. A. J. Low-band Gap Poly(di-2-thienylthienopyrazine):fullerene Solar Cells. *Appl. Phys. Lett.* **2006** *88*, 153511.

31. Klimov, V. I. Semiconductor and Metal Nanocrystals: Synthesis and Optical Properties. **2004**.

32. Efros, Al.; Efros, A. Interband Absorption of Light in a Semiconductor Sphere. *Sov. Phys. Semicond.* **1982** *16*, 772.

33. Ekimov, A.; Efros, Al.; Onushchenko, A. *Solid State Commun.* **1985** *56*, 921.

34. Brus, L. Electron-electron and Electron-hole Interactions in Small Semiconductor Crystallites: The Size Dependence of the Lowest excited Electronic State. *J. Chem. Phys.* **1984** *80*, 4403.

35. Fojtik, A.; Weller, H.; Koch, U.; Henglein, A. Photo-Physics of Extremely Small CdS Particles: Q-state CdS and Magic Agglomerations Numbers. *Ber. Bunsenges Phys. Chem.* **1984** *88*, 969.

36. Gaponenko, S. V. Optical Properties of Semiconductor Nanocrystals. Cambridge University Press 1998.

37. Wise, F. Lead Salt Quantum Dots: the Limit of Strong Quantum Confinement. *Acc. Chem. Res.* **2000** *33*, 773-780.

38. Cho, K. S.; Talapin, D. V.; Gaschler, W.; Murray, C. B. Designing PbSe Nanowires and Nanorings through Oriented Attachment of Nanoparticles. . *Am. Chem. Soc.* 2005 *127*, 7140 -7147.

39. Greenham, N. C.; Peng, X.; Alivisatos, A. P.Charge separation and transport in conjugated-polymer/semiconductor-nanocrystal composites studied by photoluminescence quenching and photoconductivity. *Physical Review B* **1996** *54*, 17628-17637.

40. Ginger, D. S.; Greenham, N. C. Charge injection and transport in films of CdSe nanocrystals. *J. of Appl. Phys.* **2000** *87*, 1361-1368.

41. Huynh, W. U.; Dittmer, J. J.; Alivisatos, A. P. Hybrid nanorod-polymer solar cells. **2002** *295*, 2425-2427.

42. Huynh, W. U. ; Dittmer, J. J.; Teclemariam, N. ; Milliron, D. J.; Alivisatos, A. P.; Barnham, K. W. J. Charge transport in hybrid nanorod-polymer composite photovoltaic Cells. *Phys. Rev. B* **2003** *67*, 115326.

43. Leatherdale, C.; Kagan, C.; Morgan, N.; Empedocles, S.; Kastner, M.; Bawendi, M. Photoconductivity in CdSe Quantum Dots Solids. *Phys. Rev. B.* **2000** *62*, 2669.

44. Maria, A.; Cyr, P. W.; Klem, E. J. D.; Levina, L.; Sargent, E. H. Solution-processed Infrared Photovoltaic Devices with >10% Monochromatic Internal Quantum Efficiency. *Appl. Phys. Lett.* **2005** *87*, 213112.

45. Zhang, S.; Cyr, P. W.; McDonald, S. A.; Konstantatos, G.; Sargent, E. H. Enhanced Infrared Photovoltaic Efficiency in PbS Nanocrystal/Semiconducting Polymer Composites: 600-fold Increase in Maximum Power Output via Control of the Ligand Barrier. *Appl. Phys. Lett.* **2005** *87*, 233101**.**

46. Neaman, D. A. Semiconductor Physics and Devices: Basic Principles. *McGraw-Hill*, 3rd edtion.

47. Clifford, J. P.; Johnston, K. W.; Levina, L.; Sargent, E. H. Shottky Barriers to Colloidal Quantum Dot Films. *Appl. Phys. Lett.* **2007** *91*, 253117.

48. Johnston, K. W.; Pattantyus-Abraham, A. G.; Clifford, J. P.; Myrskog, S. H.; Hoogland, S.; Shukla, H.; Klem, E. J. D.; Levina, L.; Sargent, E. H. Efficient Schottky-quantum Dot Photovoltaics: the Roles of Depletion, Drift, and Diffusion. *Appl. Phys. Lett.* **2008** *92*, 122111.

49. Talapin, D. V.; Murray, C. B. PbSe Nanocrystal Solids for n- and p-channel Thin Film Field-effect Transistors. *Science* **2005** *310*, 86-89.

50. Briones, F.; Golmayo, D.; Ortiz, C. The Role of Oxygen in the Sensitization of Photoconductive PbSe films. *Thin Solid Films* **1981** *78*, 385-395.

51. Jones, R. H. The Reaction of Oxygen with Lead Selenide. **1957**.

52. Yu, C. W.; Guyot-Sionnest, P. N-type Conducting CdSe Nanocrystal Solids. *Science* **2003** *300*, 1277-1280.

53. Klem, E. PhD Thesis 2008 (University of Toronto, Sargent Group).

54. Luther, J. M.; Law, M.; Song, Q.; Perkins, C. L.; Beard, M. C.; Nozik, A. J. Structural, Optical, and Electrical Properties of Self-assembled Films of PbSe Nanocrystals Treated with 1,2-ethanedithiol. *ACS Nano* **2008** *2*, 271-280.

55. Hines, M. A.; Scholes G. D. Colloidal PbS Nanocrystals with Size-tunable Near-infrared Emission: Observation and Post-synthesis Self-narrowing of the Particle Size Distribution. *Adv. Mater.* **2003** *15*, 1844-1849.

56. Murray, C. B.; Sun, S.; Gaschler, W.; Doyle, H.; Betley, T. A.; Kagan, C. R. Colloidal Synthesis of Nanocrystals and Nanocrystal superlattices. *IBM J. Res. & Dev.* **2001** *45*, 1.

57. Murray, C. B.; Kagan, C. R.; Bawendi, M. G. Synthesis and Characterization of Monodisperse Nanocrystals and Close-packed Nanocrystal Assemblies. *Annu. Rev. Mater. Sci*. **2000** *30*, 545.

58. La Mer V. K.; Dinegar, R. H.; *J. Am. Chem. Soc.* **1950** *72*, 4847.

59. Ginger, D. S.; Greenham, N. C. Charge Injection and Transport in Films of CdSe Nanocrystals. *J. Appl. Phys*. **2000** *87*, 1361-1368.

60. Oertel, D. C.; Bawendi, M. G.; Arango, A. C.; Bulovic, V. Photodetectors Based on Treated CdSe Quantum-dot Films. *Appl. Phys. Lett.* **2005** *87*, 213505.

61. Yu, D.; Wehrenberg, B. L.; Jha, P.; Ma, J.; Guyot-Sionnest, P. Electronic Transport of *n*-type CdSe Quantum Dot Films: Effect of Film Treatment. *J. Appl. Phys.* **2006** *99*, 104315.

62. Talapin, D. V.; Murray, C. B. PbSe Nanocrystal Solids for n- and p-channel Thin Film Field-effect Transistors. *Science* **2005** *310*, 86-89.

63. Murphy, J. E.; Beard, M. C.; Nozik, A. J. Time-Resolved Photoconductivity of PbSe Nanocrystal Arrays. *J. Phys. Chem. B* **2006** *110*, 25455-25461.

64. Dadosh, T.; Gordin, Y.; Krahne, R.; Khivrich, I.; Mahalu, D.; Frydman, V.; Sperling, J.; Yacoby, A.; Bar-Joseph, I. Measurement of the Conductance of Single Conjugated Molecules. *Nature* **2005** *436*, 677-680.

65. Ouyang, M.; Awschalom, D. Coherent Spin Transfer between Molecularly Bridged Quantum Dots. *Science* **2003** *301*, 5636, 1074-1078.

66. Juska, G.; Arlauskas, K.; Viliunas, M.; Kocka, J. Extraction Current Transients: New Method of Study of Charge Transport in Microcrystalline Silicon. *Phys. Rev. Lett.* **2000** *84*, 4946-4949.

67. Naka, S.; Okada, H.; Onnagawa, H.; Tsutsui, T. High Electron Mobility in Bathophenanthroline. *Appl. Phys. Lett.* **2000** *76*, 2, 197-199.

68. Mahan, J. E.; Ekstedt, T. W.; Frank, R. I.; Kaplow, R. Measurement of Minority Carrier Lifetime in Solar Cells from Photo-Induced Open-circuit Voltage Decay. *IEEE transactions on electron devices* **1979** *ED-26*, 733-739.

69. Mentzel, T. S.; Porter, V. J.; Geyer, S.; MacLean, K.; Bawendi, M. G.; Kastner, M. A. Charge Transport in PbSe Nanocrystal Arrays. *Phys. Rev. B* **2008 77**, 075316.

70. Shukla, H. Conducting Nanocrystal Solids for OptoElectronic Devices. Masc thesis 2007 (University of Toronto, Sargent Group).